

**A FIDUCIAL-BASED AUTOMATIC REGISTRATION
METHOD FOR X-RAY IMAGING FUSED WITH MRI**

by

Merdim SÖNMEZ

B.Sc, Electric-Electronic Engineering, METU, 2004

Submitted to the Institute of Biomedical Engineering
in partial fulfillment of the requirements
for the degree of
Master of Science
in
Biomedical Engineering

Boğaziçi University

Month 2008

**A FIDUCIAL-BASED AUTOMATIC REGISTRATION
METHOD FOR X-RAY IMAGING FUSED WITH MRI**

APPROVED BY:

Assoc.Prof.Dr Cengizhan Öztürk

(Thesis Advisor)

Prof.Dr Ahmet Ademoğlu

Assoc.Prof.Dr Kubilay Aydın

DATE OF APPROVAL: 25.01.2008

ACKNOWLEDGMENTS

I would like to express my sincere gratitude to Assoc.Prof.Dr Cengizhan Öztürk for providing me the opportunity to work in his lab (BUMIL) and for providing constant encouragement throughout this study. He provided me a perfect balance between guidance and freedom during my master thesis.

I am grateful to Dr. Robert Lederman, for his support and trust. He provide me opportunities to conduct animal experiments in the Cardiology Branch of NHLBI-National Institutes of Health(NIH), Bethesda, Maryland, US.

I want to thank Christine Lorenz,Ph.D., she was my co-advisor in Siemens Corporate Research, NJ, US. She was always kind and understandable. I were able to use all the necessary software and facilities of Siemens.

I wish also to thanks Akin Yüçetaş, Özgür Kocatürk, Anthony Faranesh, June Hong Kim. They shared invaluable ideas with me.

Finally, I would like to thank my mother and father, also lovely sister, without their support and love this thesis would not be possible.

ABSTRACT

A FIDUCIAL-BASED AUTOMATIC REGISTRATION METHOD FOR X-RAY IMAGING FUSED WITH MRI

X-ray fluoroscopy is widely used in image-guided interventions especially in catheter-based interventions. X-ray fluoroscopy provides high temporal and spacial resolution, but it suffers from low soft tissue contrast. On the other hand, magnetic resonance imaging (MRI) offers excellent soft tissue contrast and 3D anatomical information. X-ray fused with MRI (XFM) is a system which combines strengths of both image modalities to improve the quality of image-guidance and to achieve minimally invasive interventions. In XFM, pre-operative MR images are segmented, 3D structure of target area is reconstructed from these segments, its 2D projection is overlapped on top of live images during x-ray fluoroscopy. Fusion of two images requires registration of two images which could be achieved using external fiducial markers attached to skin of patient. In this approach, first markers are detected and located in both image sets, then least square minimization algorithm is applied to complete the registration. The purpose of our study is to extend the currently practiced XFM systems and to allow its translation into a practical clinical setting by making it easier to use. We developed a fully automatic registration system for XFM. This includes automatic segmentation and localization of fiducial markers in both images and finding the correspondence between two point sets, also designing a marker localization system and development of user interface for technical user. In vivo validation of our method was performed in 10 animal experiments. Results show that our method locates markers in high accuracy, finds correspondence between two point sets and completes the registration process.

Keywords: Image-Guided Intervention, Image Registration, X-Ray Fused with MRI, Correspondence Between Point Sets.

ÖZET

OTOMATİK YÖNTEMLE GÜVENİLİR İŞARETLEYİCİYE DAYALI X-IŞINI ve MR GÖRÜNTÜLERİNİN KAYNAŞTIRILMASI

X-ışını görüntüleme özellikle kateter ile yapılan girişimlerde yaygın olarak kullanılmaktadır. X-ışını, yüksek çözünürlük ve yüksek görüntü yenileme hızı sağlamakla birlikte, yumuşak doku kontrastına sahip değildir. Diğer taraftan, MR görüntüleme (MRG) mükemmel yumuşak doku kontrastı ve 3 boyutlu anatomik görüntü sağlayabilmektedir. Her iki görüntülemenin özelliklerinin birleştiren X-ışını ve MR görüntü kaynaştırması (XMK), yüksek kalitede görüntüleme elde etmekte ve minimum düzeyde girişimsel ameliyatlara gerçekleştirmektedir. Önceden çekilmiş MR görüntüleri bölütlenir, hedef bölgenin 3 boyutlu yapısı bu bölütlerden inşa edilir, bu 3 boyutlu yapının 2 boyutlu projeksiyonu ameliyat sırasında canlı alınan X-ışını görüntülerinin üstüne konarak kaynaştırılır. Kaynaştırma işlemi için her iki imge çakıştırılmalıdır, bu işlem için hastanın derisine tutturulmuş güvenilir işaretleyiciler kullanılır. Güvenilir işaretleyiciler her iki imgede de tespit edilir ve yerleri belirlenir, iki işaretleyici setine aralarındaki mesafeyi en küçük karelerle küçülten algoritma uygulanır ve çakıştırma işlemi tamamlar. Bizim bu çalışmadaki ana amacımız XMK sistemlerinin geliştirmek ve basitleştirerek klinik uygulamalara geçişini sağlamak. XMK için tam otomatik bir çakıştırma sistemi geliştirmeyi amaçladık. Bu sistem, güvenilir işaretleyicilerin otomatik bölütlenmesini ve yerinin belirlenmesini, her iki imgedeki imleyiciler arasındaki eşleşmenin otomatik bulunmasını, işaretleyici yerleştirme sistemini ve teknik kullanıcılar için ara yüz programını içermektedir. Geliştirdiğimiz metotların doğruluğu 10 hayvan deneyinde test edilmiştir. Sonuçlar gösterdi ki yöntemlerimiz işaretleyicileri yüksek doğrulukla bulmakta, eşleşmeleri hesaplamakta ve çakıştırmayı tamamlamaktadır.

Anahtar Sözcükler: Görüntü Destekli Müdahale, Görüntü Çakıştırma, X-ışını ve MR Görüntü Kaynaştırılması, Nokta Kümelerini Eşleştirme

TABLE OF CONTENTS

ACKNOWLEDGMENTS	iii
ABSTRACT	iv
ÖZET	v
LIST OF FIGURES	viii
LIST OF TABLES	xi
LIST OF ABBREVIATIONS	xii
1. Background	1
1.1 Image Guided Interventions	1
1.1.1 X-Ray-Guided Interventions	1
1.1.2 CT-Guided Interventions	2
1.1.3 MRI-Guided Interventions	3
1.2 Overview of Image Registration	3
1.2.1 Point-Based Registration	4
1.2.2 Intensity-Based Registration	4
1.2.3 Feature-Based Registration	6
1.3 Image Fusion Technics and Applications	7
1.3.1 PET-CT Fusion	7
1.3.2 X-Ray MRI Fusion	8
1.4 X-Ray Fused with MRI (XFM)	9
1.4.1 Fiducial Markers	11
1.4.2 Imaging	11
1.4.3 Distortion Correction	11
1.4.3.1 Distortion Correction of MR Images	11
1.4.3.2 Distortion Correction of X-Ray Images	11
1.4.3.3 Geometry Calibration of C-arm	12
2. Automatic Registration for X-Ray Fused with MRI System	15
2.1 Introduction	15
2.2 Methods and Materials	17
2.2.1 X-Ray Side Fiducial Marker Detection	17

2.2.2	MRI Side Fiducial Marker Detection	19
2.2.3	Correspondence Between Two Point Sets	22
2.3	Results	24
2.3.1	X-Ray Side Fiducial Marker Detection	24
2.3.2	MRI Side Fiducial Marker Detection	26
2.3.3	Correspondence Between Two Point Sets	26
2.4	Discussion and Conclusions	26
3.	Clinical Applications	31
3.1	Baseline MRI	31
3.2	Results	32
3.2.1	Case Example: Roadmaps From Contrast-Enhanced MR An- giograms	32
3.2.2	Case Examples: Iliac Artery Revascularization and Registration Error	33
3.2.3	Case Example: Coronary Arteriography, Ventriculography, and ECG-Gated XFM	34
4.	Conclusion	36
4.1	Future Works	38
	APPENDIX A. Algorithm of Finding Correspondence Between 3D Point Sets	39
	APPENDIX B. Auto-Registration User Interface	41
	REFERENCES	43

LIST OF FIGURES

Figure 1.1	Iterative algorithm for 2D-3D intensity-based registration of x-ray and CT images. (taken from [20]).	5
Figure 1.2	3D reconstructed anatomical structure, blood vessel, is registered with x-ray images by a using feature-based registration method. Skelotonised structures are generated for 3D and x-ray images to find correspondence between sub-point set using a territory-based correspondence search (taken from [24]).	7
Figure 1.3	Image (A) is CT images, image (B) is CT fused PET. Tumor tissue is obviously detected in this image.	8
Figure 1.4	Figure shows flow diagram of XFM system. Markers are identified both in x-ray and MRI images and 3D locations of markers are determined. Least square minimization algorithm is applied these marker sets to align two point set and find transformation parameters. Segmented and reconstructed MR images are transformed to x-ray space and projected on top of x-ray images	10
Figure 1.5	Grid phantom is used to observe the distortion characteristic in x-ray images. Image (A) is before and (B) is after distortion correction. Black line is added to highlight the distortion(taken from [32]).	12
Figure 1.6	Reconstructed 3D metal beads are back projected on x-ray images. Image(A) without calibration. Image(B) with just in-plane rotation was calibrated. Image (C) both rotation and translation were calibrated (taken from [31]).	14
Figure 2.1	Attachment system of markers to the patient. Elastic velcro vest is designed to eliminate undesirable shifting of the fiducial markers.	16

Figure 2.2	Distance between center of markers (X) detected by canny edge detection and center of markers (O) detected by bothat filter was determined. If centers are closer than a threshold then center of markers (X) detected by canny edge detection were assigned as a real marker(.)	18
Figure 2.3	A search radius R_{search} is defined and a circle is constructed to find candidate markers in consecutive frame	20
Figure 2.4	Markers with in the search circle are found and their properties are compared	21
Figure 2.5	Maximum intensity projections of volumetric MR images on transverse (A), sagittal (B), coronal (C) direction and segmented markers (D)	22
Figure 2.6	Detected and 3D reconstructed x-ray side fiducial markers are back projected to each frames to verify the results.	25
Figure 2.7	Automatically detected MRI side fiducial markers are back projected to MIP of 3D volume to verify the results.	27
Figure 3.1	XFM using a 3D contrast-enhanced MR angiogram. (A) shows a retrograde L iliac radiocontrast angiogram in a contralateral oblique projection. (B) shows the regions of interest (adventitial borders, green) derived from a T1-weighted noncontrast MRI. (C) shows the XFM of both x-ray and MR angiograms. The correspondence is high.	32
Figure 3.2	Unsatisfactory registration during an iliac artery revascularization procedure. Panel A shows the misregistration of a contrast-enhanced MR angiogram with x-ray during XFM. Multiple fiducial markers are positioned on the abdominal skin. Panel B shows another patient with MR-derived arterial adventitial contours overlaid during recanalization of occlusive iliac in-stent restenosis. Both presumably reflect error introduced by nonrigid deformation and respiratory motion of the fiducial markers.	33

- Figure 3.3 XFM during graft coronary arteriography. An injection sequence of a right internal mammary artery during ECG-gated XFM with continuous table panning. The corresponding numbered phase of the cardiac cycle is correctly represented by the MRI-derived regions of interest, irrespective of table position, throughout the injection. 35
- Figure B.1 Figure shows user interface for end-user to perform automatic registration process. 42

LIST OF TABLES

Table 2.1	Automatic detection algorithm was tested, in vivo animal experiments. 16 ± 2 markers which are affixed to swine body by tight vest were employed in each experiments.	28
Table 2.2	We created 3D point sets with arbitrary number of member and select some of them randomly. We applied rotational and translational transformation these selected points and also added some noise to simulate any possible noise coming from different image modalities	29

LIST OF ABBREVIATIONS

XFM	X-ray Fused with MRI
MRI	Magnetic Resonance Imaging
XF	X-ray Fluoroscopy
CT	Computed Tomography
PET	Positron Emission Tomograph
CTF	CT Fluoroscopy
DRR	Digitally Reconstructed Radiographs
PA	Primary Angle
SA	Secondary Angle
IS	Intensifier Size
SOD	Source-to-Object Distance
SID	Source-to-Intensifier Distance
II	Image Intensifier
FOV	Field Of View
MIP	Maximum Intensity Projection
FDG	Radiotracer fluorodeoxyglucose
CC	Cross-Correlation
AP	Anterior-Posterior
TRE	Target Registration Error

1. Background

1.1 Image Guided Interventions

For most of the history of medicine, physicians trusted their senses, mainly vision and touch, to diagnose illness, monitor a patient's condition, and perform invasive procedures. During the last few decades various three-dimensional medical imaging techniques, such as computed tomography (CT), magnetic resonance imaging (MRI), and ultrasound, have been developed to allow a physician to diagnose a disease that is hidden from normal view. Three-dimensional biomedical images are now being used not only for diagnosis, but for also planning and conducting new treatments such as minimally invasive surgeries. The following sections explain currently available techniques of image guidance for interventions.

1.1.1 X-Ray-Guided Interventions

Since their discovery in 1895, x-rays have been a vital scientific tool, revealing previously concealed worlds. Because of their great penetrating power, x-rays can also be used to study the structure of living organisms. One of the earliest applications of x-rays was in medicine, where they were used for both diagnosis and therapy. They penetrate soft tissues but are stopped by bones, which absorb them. Thus if a photographic plate that is sensitive to x-rays is placed behind a part of the body and an x-ray source is placed in front, x-ray exposure will result in an image of the bones and internal organs. When the radiograph, or plate, is developed, a negative image is produced. Tissues that are easily penetrated by x-rays appear dark, while bones and dense tissues show up as light or white regions.

Although bones are the most opaque structures, there are many dense tissues, such as tumors, that can also show up unusually light in radiographs. These images

can be used to study damaged or broken bones, inspect dental cavities, detect foreign objects in the body, and diagnose diseases. To utilize x-rays for the investigation of other, less dense tissues of the body, such as the gastrointestinal tract, the tissues must first be made opaque to x-rays. Generally, patients are asked to drink a mixture containing an opaque substance, such as a Barium containing mixture, so that the outline of the digestive tract becomes visible with x-rays.

In x-ray fluoroscopy, we observe a particular organ in action, such as the heart. The patient is placed in the fluoroscope between the x-ray source and a screen that is coated with a fluorescent substance. The image that appears when the x-rays strike the screen is brightened by an electronic device called an image intensifier. New x-ray system eliminates intensifier and allow direct digitization of x-ray transmission images using semiconductor technology.

1.1.2 CT-Guided Interventions

CT is the gold standard in the diagnosis of a large number of different diseases such as cerebrovascular accidents, intracranial hemorrhage in the head and pulmonary embolism. Relatively high spatial resolution and the scan speed of CT allows excellent imaging of proximal coronary arteries. Beside of its diagnostic value, CT could be used as a guide for interventional procedures to provide 3D structure of anatomy. Recent advance in CT scanner technology and computer hardware have led to the development of CT fluoroscopy (CTF), which allows real-time acquisition and display of cross-sectional images. For example in percutaneous biopsy procedures, CT-fluoroscopy makes it possible to visualize the needle trajectory from skin entry to the target point, performing the procedure more effectively and rapidly [1]. Real-time CT-fluoroscopy is valuable in assisting thoracic drainage procedure and guiding transbronchial needle aspiration [2]. On the other hand, there are some the concerns of using CT-fluoroscopy; these are the significant radiation exposure to the patient and the scattered exposure to the radiologists. It is shown that CT-fluoroscopy expose higher radiation then other methods and some preventing methods are proposed to decreased scattered exposure [3, 4, 5, 6].

1.1.3 MRI-Guided Interventions

Magnetic resonance imaging, like CT, is used in diagnostic purposes for many years in medicine. MRI provides excellent soft tissue contrast space better than CT and does not have any known hazardous effects, in contrast to CT. MRI also provides functional information of the body, therefore it is extremely useful in cardiovascular, neurological and oncological diseases. Recent advances in MR hardware, image processing techniques and MRI compatible devices allow physicians to perform real-time MRI-guided interventions. Real-time MRI-guidance is used to perform percutaneous interventions in pain therapies, which are lumbar facet joint injections, sacroiliac joint injections, lumbar spinal nerve root infiltrations and drug delivery to the lumbar sympathetic chain [7]. MR-guided pediatric interventions are a promising application area because ionizing radiation is eliminated which is more critical in children [8]. In stem cell therapy, MR-guidance is shown to provide precise targeting for cell delivery and tracking of appropriately labeled cells [9].

New generation MR scanners with wide and short bores and real-time pulse sequences made MR-guided cardiovascular interventions possible. Under MR-guidance, Speuntrup *et al.* [10] placed the stent to coronary artery which is a challenging intervention because of the artifacts due to respiratory and cardiac motions. In various animal models, transluminal [11, 12] and stent deployment [13, 14] have been successfully conducted under MR guidance.

However, there are also some difficulties with MR-guided interventions such as lack of MR compatible surgical devices, safety issues related with heating of devices and difficulties of monitoring the patient condition.

1.2 Overview of Image Registration

Medical images are being used for diagnoses, planing and guiding treatment and monitoring patient condition. There are benefits in combining and comparing

medical images, because additional medical information can be found. First step of this comparative analysis is the alignment of images. This step is also known as image registration. Many algorithms have been proposed in the last decade for medical image registration. These methods will be explained briefly in following sections.

1.2.1 Point-Based Registration

The most reliable registration method uses points which are driven from internal or external markers [15, 16, 17]. External markers are attached to the rigid structures such as bones to minimize their displacement. However, it is not always possible to fix markers this way because it is too invasive for most of the applications. In this thesis we employed this registration techniques. The fiducial points came from the centroid of the dual modality markers. Point-based registration computes rigid transformation matrix which aligns two points sets to each other. It is accurate, fast and robust, thus, it is used as a gold standard to evaluate other registration technics. One major disadvantage of point-base registration is that it is vulnerable to movement of markers when markers are attached to the skin.

1.2.2 Intensity-Based Registration

Intensity-based registration algorithms match the intensities of one image data set to another image set by minimizing a similarity measure between them. Intensity-based registration could be used to combine intraoperative fluoroscopic x-ray images with preoperative CT images. This is an easier process that what is required in XFM because both x-ray fluoroscopy and CT have same image contrast characteristics [18, 19]. Digitally reconstructed radiographs (DRR), projection of CT volume, could be used for x-ray CT registration. Registration is achieved by finding the right position and orientation with respect to the CT data, so that a DRR computed at this pose matches perfectly with the x-ray image. This requires knowledge about the geometry of the x-ray imaging device, so that the DRR can be generated using a perspective

projection. The algorithm is as following, also shown in Figure 1.1:

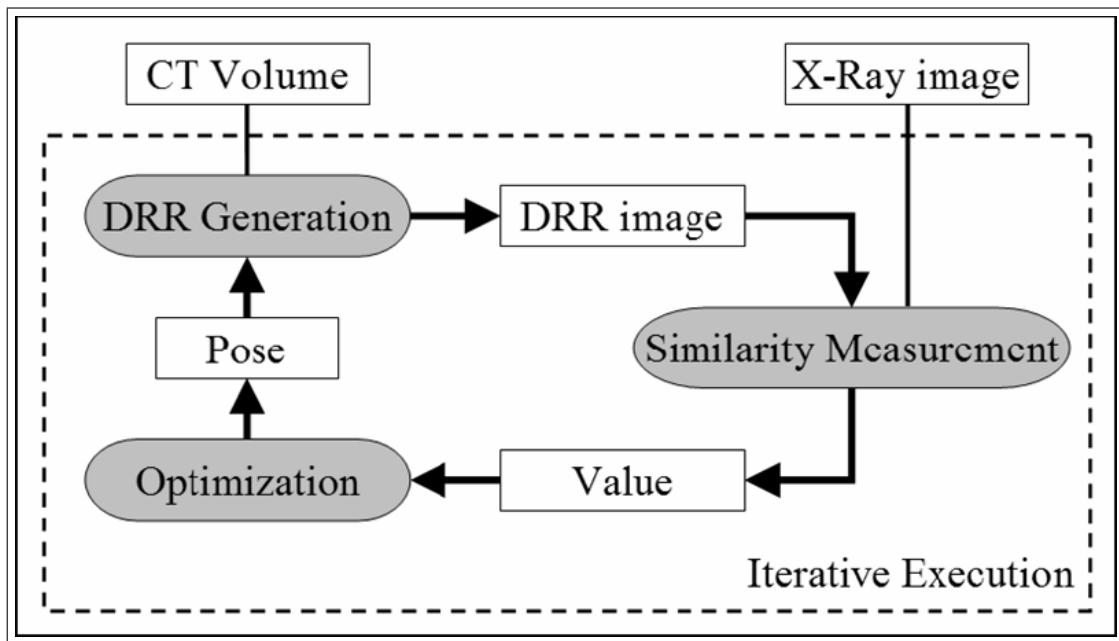


Figure 1.1 Iterative algorithm for 2D-3D intensity-based registration of x-ray and CT images. (taken from [20]).

1. The user feeds the system with a CT data set, a x-ray image, the intrinsic parameters of the x-ray imager and an initial starting estimate for the rigid transformation defining where the DRR is to be generated.
2. Using the perspective projection extracted from the intrinsic parameters of the x-ray sensor and the current value of the rigid transformation, a DRR image is computed from the CT data.
3. The alignment of this DRR and the x-ray image is assessed by a similarity measure. For an intensity-based registration, this measure operates directly on the image data and returns a single number, telling how well the images are matched.
4. This number is used as a cost function for an optimization algorithm, which alters the rigid transformation in order to achieve a better alignment. It tries to find the optimum transformation where the DRR has the maximum similarity with the x-ray image.

Intensity-based registration, however, is computationally time consuming. It requires many comparison between Digitally Reconstructed Radiographs, generated from CT, and x-ray images. Several algorithms have been proposed to speed up DRR generation [21, 22].

1.2.3 Feature-Based Registration

Feature-based registration consists of many different approaches depending on the dimensionality and the type of features. Nevertheless, most of the feature based registrations techniques can be divided into four steps.

- Feature detection
- Feature matching
- Transform model estimation
- Image transformation

The goal of feature matching is to establish correspondences between two sets of features. The problems that can occur here can be caused by an incorrect feature detection, or by image distortion. A matching algorithm has also to deal with single features i.e. features that is only seen in one image.

One of feature-based registration applications is to register 3D reconstructed anatomical structure, for example blood vessel, with x-ray images, as seen in Figure 1.2. Algorithm first generates a 'skeleton' of the blood vessels present in the x-ray image, reducing the thickness of each to a single pixel. Blood vessels in the 3D model are also 'skeletonised', by extracting the medial axis of each vessel. The algorithm then selects a sub-sample of points on the 3D skeleton model. For each 3D point, the closest corresponding point in the 'skeletonised' x-ray image is found using a territory-based

correspondence search. Using these pairs of points, the algorithm iteratively finds the optimal rotation and translation of the 3-D model to achieve a registration [23].

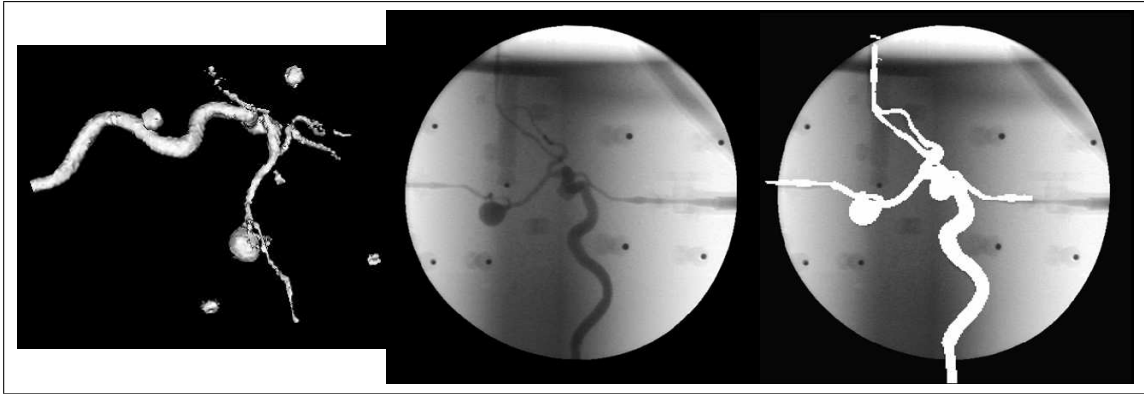


Figure 1.2 3D reconstructed anatomical structure, blood vessel, is registered with x-ray images by using feature-based registration method. Skeltonised structures are generated for 3D and x-ray images to find correspondence between sub-point set using a territory-based correspondence search (taken from [24]).

1.3 Image Fusion Technics and Applications

1.3.1 PET-CT Fusion

The goal of the positron emission topography (PET) is to generate images of the distribution of positron emitters *in vivo*. PET system rely on the detection of annihilation gamma rays in coincidence by detectors that surround the patient. PET scans are used most often to detect cancer and to examine the effects of cancer therapy by characterizing biochemical changes in the cancer. PET scans of the heart can be used to determine blood flow to the heart muscle and help evaluate signs of coronary artery disease. PET scans of the brain are used to evaluate patients who have memory disorders of an undetermined cause, suspected or proven brain tumors or seizure disorders that are not responsive to medical therapy and are therefore candidates for surgery. The spatial resolution of PET is around 5mm and is limited by the fundamental nature of positron annihilation. On the other hand, CT imaging offers high resolution, routinely with 1mm pixel spacing and 3D anatomical images. PET-CT fusion therefore provides excellent guidance for cancer or tumor biopsy or surgery procedures.

PET with CT imaging-with the radiotracer fluorodeoxyglucose (FDG)-enables the collection of both biological and anatomical information during a single exam, with PET picking up metabolic signals of tissues and CT offering a detailed map of internal anatomy [25]. FDG PET-CT offers several advantages over PET alone; the most important is the ability to accurately localize increased FDG activity to specific normal or abnormal anatomic locations,as shown in Figure 1.3 .

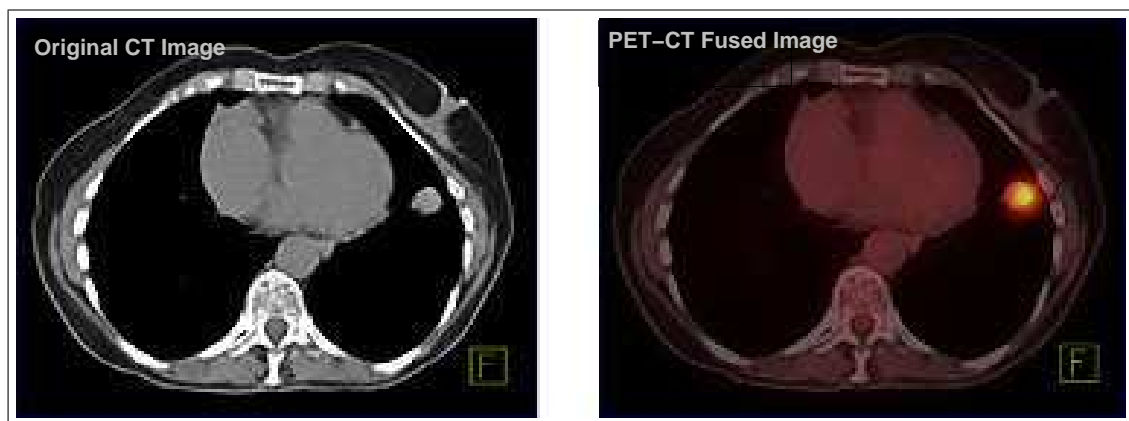


Figure 1.3 Image (A) is CT images, image (B) is CT fused PET. Tumor tissue is obviously detected in this image.

1.3.2 X-Ray MRI Fusion

X-ray and MR images are complementary images, where x-ray imaging has high temporal and spatial resolution and MRI has soft tissue contrast and 3D anatomical information. Fusion of these two modalities could provide excellent guidance in catheter-based intervention. There have been several efforts which aim to combine x-ray and MR images. These will be introduce here, our approach will be explained in detail in the next section (Section 1.4).

Fahrig *et al.* [26, 27, 28] employed a combined system which contains a stationary flat-panel XF within an open 0.5T MR scanner. He has conducted some successful live case studies. Since both system is combined on a single table and both image sets are in the same space which enables one time registration process which is relatively

easy. However, static, fixed-angle XF limits the applications and low Tesla magnetic scanner decreases image quality. In a different XMR system, Rhode *et al.* used mobile C-arm and 1.5T MR scanner in an same operation room which consist of sliding table between two scanner [29, 30]. They register two image spaces using infrared emitting diodes attached to sliding table and C-arm of XF. They tracked position of table and orientation of C-arm with special tracking device which eliminates the need of segmentation of any markers. However, they register two systems independent from the patient. This makes their system vulnerable to patient movement.

1.4 X-Ray Fused with MRI (XFM)

Physician uses x-ray fluoroscopy (XF) to visualize the maneuver of the catheter through the body structure especially in arteries and veins. XF provides high spatial resolution and temporal resolution which is ideal for catheter-based procedures. Unfortunately, x-ray fluoroscopy suffers from lack of soft tissue contrast. X-ray attenuations of body structures, except bone, are very close to each other, and it is very difficult to distinguish these structures from each other. Another disadvantage of x-ray fluoroscopy is that it requires the use of radio-opaque contrast agent to highlight vessels, the main structure of interest. MRI, in contrast to x-ray imaging, offers excellent soft tissue contrast. It is commonly used to demonstrate pathological or the physiological alternation of tissues. 3D volume images or 2D plane images with arbitrary orientation can be acquired using MRI. However, MR imaging has also some disadvantages, when it is compared with x-ray: it has a relatively slower acquisition rate, resolution of MRI images is lower and it is very sensitive motion during the image acquisition. Furthermore, most of the catheters and other tools used during the surgery are not compatible with the high magnetic field of an MR scanner. While both imaging modalities are suffering from drawbacks, a solution to overcome some of the individual problems could be to register and fuse both images while doing interventions. X-ray fused with MRI (XFM) is such a system which combines the strengths of both modalities to improve quality of image guidance. In this system, a priori MR images of the subject are overlaid on top of the live images acquired during x-ray fluoroscopy. Accurate regis-

tration of two image modalities is necessary to achieve this and we employ external fiducial markers which are attached to the skin of the subject with a tight-fitting vest minimizing unwanted marker motion. Flow diagram of XFM is shown in Figure 1.4. Following subsections explain basic steps components of XFM. Purpose of our study is to extend XFM system and to enable its translation into a practical clinical setting. We proposed to achieve a fully automatic registration system for XFM. This includes detection and segmentation of fiducial markers in both image modalities and finding the correspondence between two data sets.

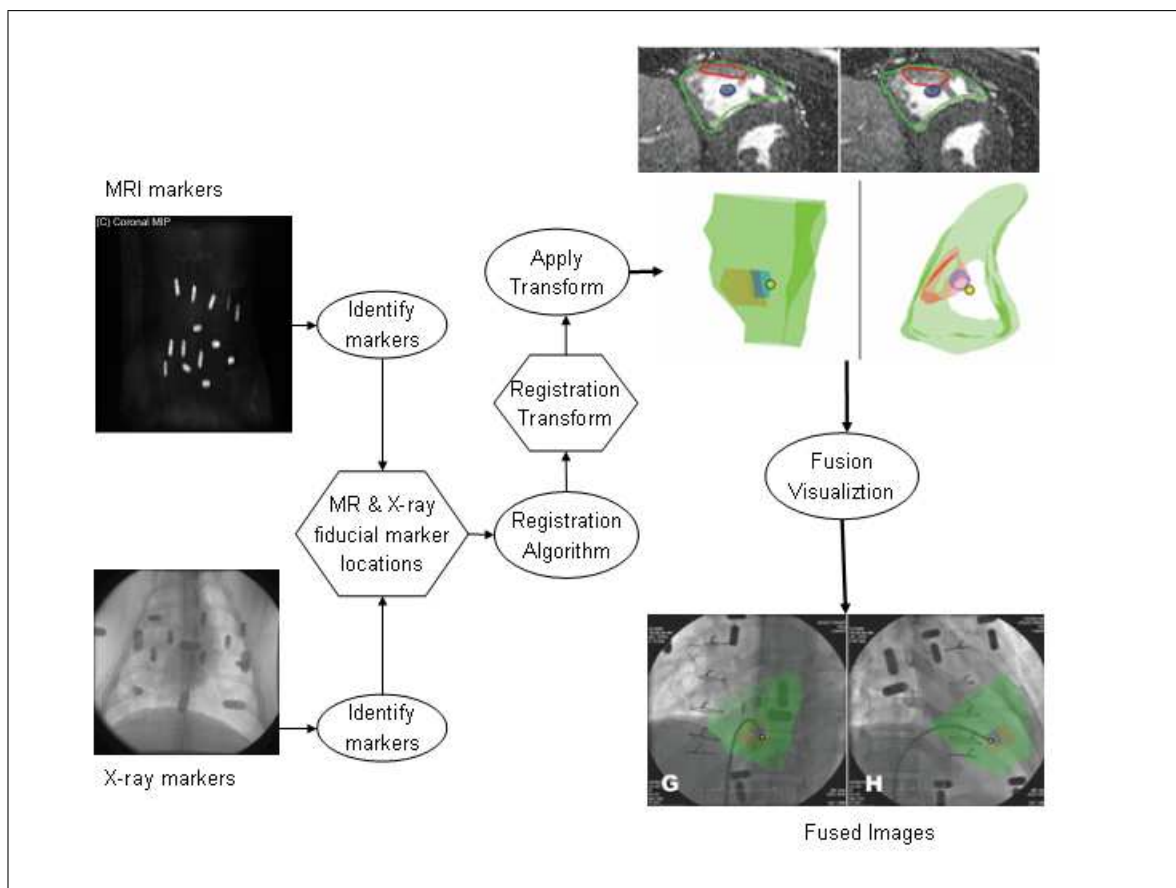


Figure 1.4 Figure shows flow diagram of XFM system. Markers are identified both in x-ray and MRI images and 3D locations of markers are determined. Least square minimization algorithm is applied these marker sets to align two point set and find transformation parameters. Segmented and reconstructed MR images are transformed to x-ray space and projected on top of x-ray images

1.4.1 Fiducial Markers

XFM relies on the matching of fiducial markers. Markers are ellipsoidal shape plastic capsules filled with with a multi-modality contrast solution (Beekley Corporation, Bristol, CT, US). Solution is 5mM Gd-DTPA (Magnevist, Berlex, Montville, NJ, US) in iodinated contrast solution (Visipaque, Amersham Health, Buckinghamshire, UK).

1.4.2 Imaging

Images were acquired from Axiom Artist cardiac single plane XF system and 1.5 T Siemens Sonata MR scanner. These two system are connected by sliding table which transfers patient from one imaging system to another. Position of markers in MR space was determined by using 3D gradient echo image with following parameters: TR/TE, 2.37/1.18 ms; flip angle, 17°; FOV, 400 × 300 × 230 mm; matrix, 256 × 192 × 61 voxels; bandwidth, 1300 Hz/pixel. XF system uses conventional image intensifier (II) with maximum field of view (FOV), and images were acquired in 512 × 512 pixels format.

1.4.3 Distortion Correction

1.4.3.1 Distortion Correction of MR Images. MR imaging is based on linear magnetic gradients within the bore of the magnet. However, the gradients are non-linear at the edge of the imaging volume and not constant in the z-direction, causing image distortion. All these distortions are corrected with software supplied by Siemens.

1.4.3.2 Distortion Correction of X-Ray Images. X-ray images suffer from pin-cushion and S-shaped geometric distortion, as shown in Figure 1.5. S-shaped geometric distortion is due to local magnetic field and has both rotational and translation com-

ponents and depends on position of C-arm. Gutierrez in his Ph.D. thesis explains a global solution for x-ray image distortion [31]. Phantom used to for characterization the distortion was a sheet of plastic with metal rings placed in a regular grid pattern. Images were acquired from PA=-50° to PA=50° with 5° inclement. The rings were segmented for each image. 5th-order polynomial coefficients were determined that fits distorted ring image to ideal grid image. Using these coefficient x-ray images corrected for a given angle within the calibration range.

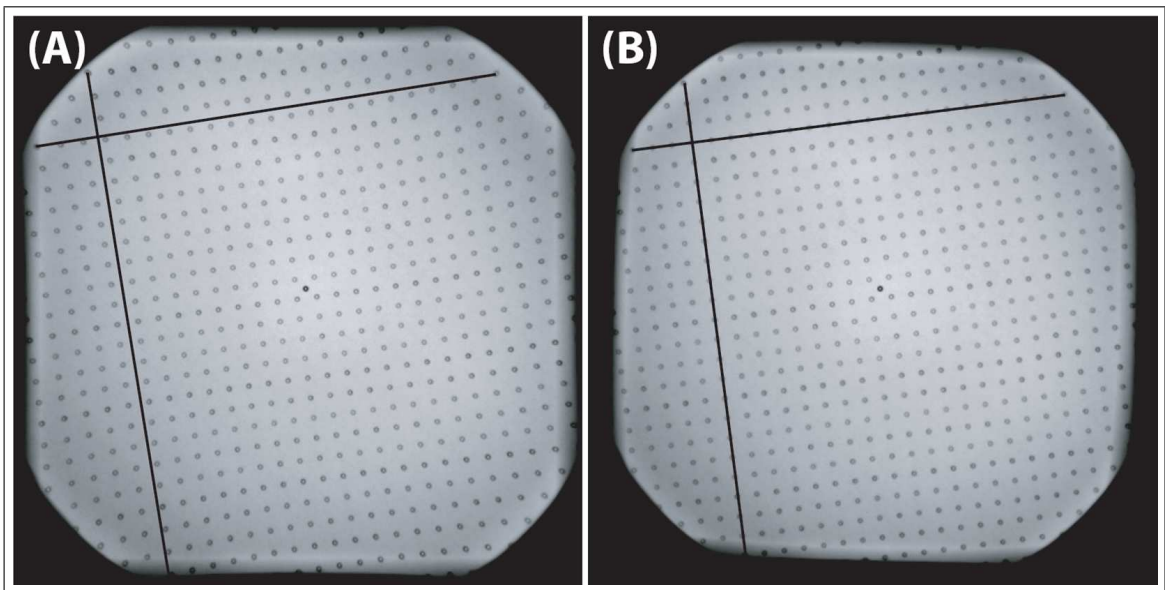


Figure 1.5 Grid phantom is used to observe the distortion characteristic in x-ray images. Image (A) is before and (B) is after distortion correction. Black line is added to highlight the distortion(taken from [32]).

1.4.3.3 Geometry Calibration of C-arm. There is also low order distortions introduced by the II in x-ray images. When 3D images are projected to 2D images rotational and translational distortion are observed. 3D-to-2D image projection is obtained by the following equations:

$$\begin{bmatrix} x_n \\ y_n \\ z_n \end{bmatrix} = \begin{bmatrix} -I_i \frac{SID}{FOV} & 0 & -I_i/2 \\ 0 & -I_j \frac{SID}{FOV} & -I_j/2 \\ 0 & 0 & 1 \end{bmatrix} \begin{bmatrix} x_m \\ y_m \\ z_m \end{bmatrix} \quad (1.1)$$

and

$$\begin{bmatrix} i \\ j \end{bmatrix} = \begin{bmatrix} x_n/z_n \\ y_n/z_n \end{bmatrix} \quad (1.2)$$

where n refers to XF 2D coordinates, m refers to local XF 3D coordinates, I_i and I_j are number of pixel in i and j direction, and (i,j) are the image coordinates. Gutierrez *at el* [31] added an extra step to simulate residual in-plane rotation and translation caused by distortion:

$$\begin{bmatrix} i' \\ j' \end{bmatrix} = R' \begin{bmatrix} i \\ j \end{bmatrix} + t' \quad (1.3)$$

where R' and t' are 2D rotational and translation matrix, (i', j') is the new coordinate due to distortion.

A phantom containing 19 metal beads with known dimension was constructed to recover these distortions. Images were acquired from PA=-45° to PA=45° with 15° increment. 3D position of these beads were reconstructed. 3D reconstructed coordinates were back projected each images and by minimizing distance between actual beads and projected beads, the geometric calibration parameters were determined. Applying these parameters to 3D-to-2D projection improve the quality of projection, as shown in Figure 1.6

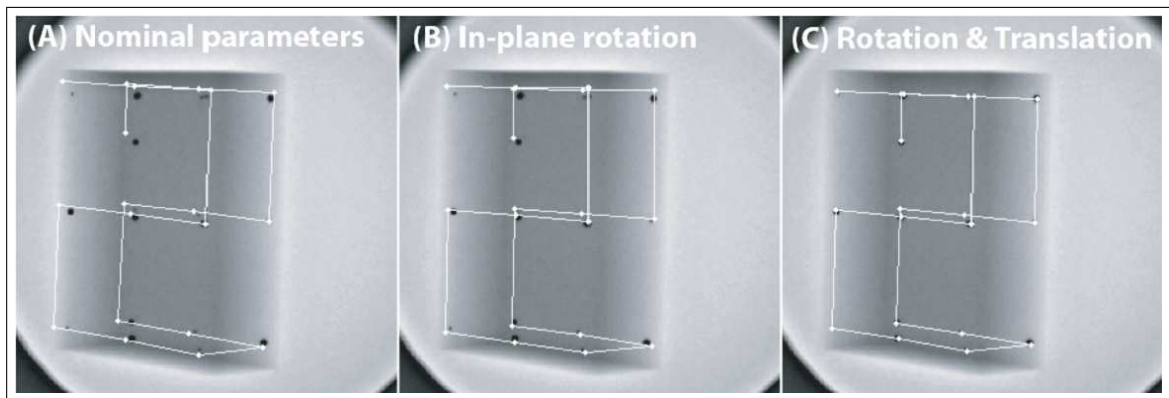


Figure 1.6 Reconstructed 3D metal beads are back projected on x-ray images. Image(A) without calibration. Image(B) with just in-plane rotation was calibrated. Image (C) both rotation and translation were calibrated (taken from [31]).

2. Automatic Registration for X-Ray Fused with MRI System

2.1 Introduction

In this study we present a fully-automatic fiducial marker-based registration system for XFM. This encompasses detection of markers in both MR and x-ray images, reconstruction of 3D position of markers and finding correspondence between 3D point sets automatically. As it is mentioned in section 1.4 these steps were performed manually or semiautomatically in previous studies. We aim to simplify the registration steps for routine clinical use by making the system fully automatic.

Automatic detection of markers needs different approaches for each image modality due to their varying image characteristics. X-ray images are 2D but formed by a projection of the 3D space, causing occasional overlapping of markers. This problem could be overcome by acquiring multiple x-ray images with different angles. In this study, we acquired x-ray images in a constant rotational sweep of the C-arm. In contrast to x-ray, MR imaging modality is intrinsically in 3D space and has no overlapping problem. It also requires robust and accurate segmentation routines for marker detection. Since markers were attached around the body and in our typical application distributed to lateral, anterior and posterior surfaces, identification of markers could be directed at these regions.

After markers are identified in both MR and x-ray images, matching of these point sets is required to complete registration. In this thesis, a novel algorithm is proposed as a solution for marker matching. This correspondence algorithm is based on triangle similarity. All possible triangle sets were built from marker sets and each triangle from first set is compared with all other triangles from other set. From the similarity of the triangles a confidence value is obtained for each match and assigned to the corners of these two triangles. Cumulative confidence value coming from all possible matches are constructed in this matter for all possible corner matches in a

matrix form. This matrix provided the correspondence between two point sets and 3D-to-3D registration was performed. This process is explained in detailed in section 2.2.3

Beside of software algorithm, we have also developed a marker placement system and user interface for end-users to perform automatic registration. Marker displacement is a serious problem especially in patients with loose skin, we designed a vest from elastic fabric and velcro to eliminate this displacement, as shown in Figure 2.1. Information about our automatic registration software user interface which is written in Matlab is presented in Appendix B.

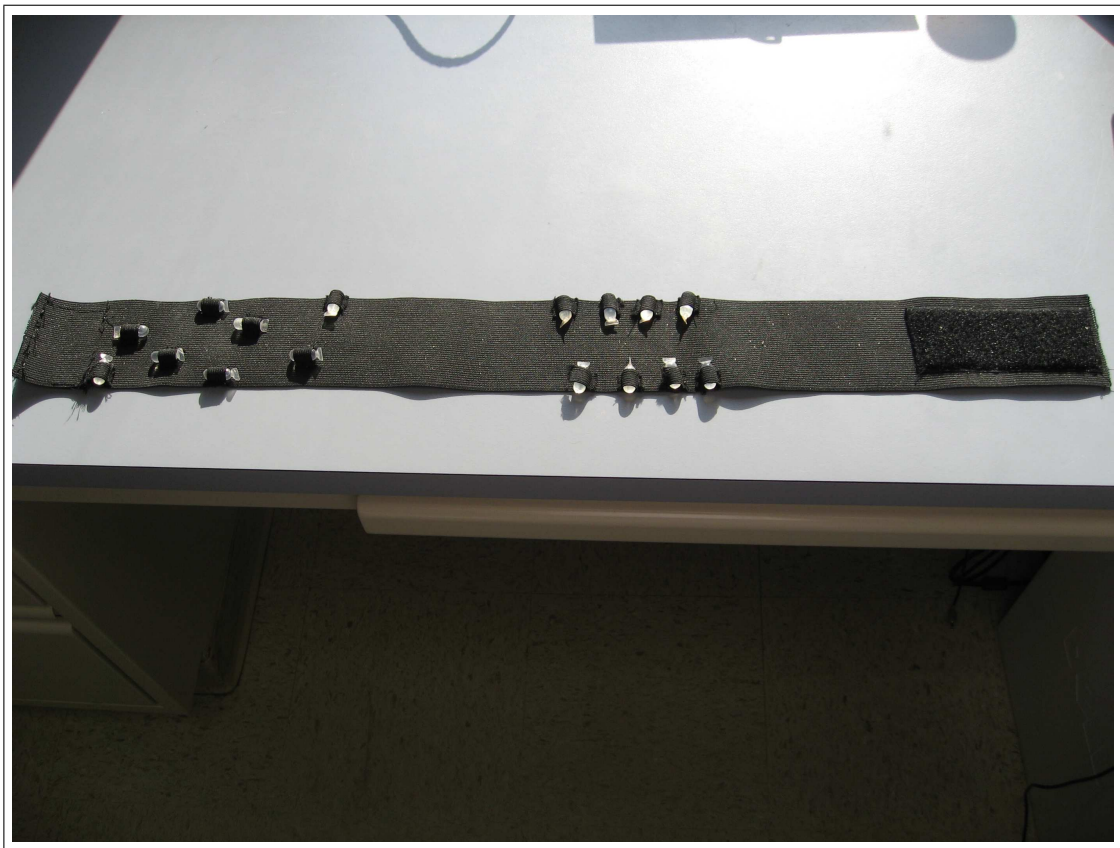


Figure 2.1 Attachment system of markers to the patient. Elastic velcro vest is designed to eliminate undesirable shifting of the fiducial markers.

2.2 Methods and Materials

2.2.1 X-Ray Side Fiducial Marker Detection

X-ray images were acquired using an Axiom Artis cardiac single plane XF system (Siemens, Erlangen, Germany) and the live fluoro images are captured by a frame grabber and saved to an external workstation running MATLAB. The following parameters were used in our study to describe x-ray imaging modality. Primary angle (PA) describes rotation of C-arm around the long axis of the patient from left to right. Secondary angle (SA) represent rotation of C-arm around the left-right axis of the patient from head to feet. IS is the intensifier size, SOD is the source-to-object (isocenter) distance, and SID is the source-to-intensifier distance.

Due to the projection-type image characteristic of x-ray and since external fiducial markers were both placed on anterior and posterior surfaces of patient, there may be some overlapped marker in images, as seen Figure 2.2. Multiple images with different angles were acquired to solve this problem. An automatic rotational scan option of the AX system was utilized to acquire views whose primary angle, α , ranges from -30° to $+30^\circ$ (secondary angle, β , was unchanged and kept at 0°) with $\Delta\alpha=3^\circ$ angle increment. In total $N=21$ images are obtained: $\alpha=\{0^\circ, \pm 3^\circ, \dots, \pm 30^\circ\}$. These images were first processed to detect marker candidates at each frame, later analyzed jointly to find matching markers between frames and to reconstruct 3D position of markers in x-ray side.

Automatic detection of markers requires advance image processing techniques and double check mechanisms to have reliable results. We first applied 2 different detection algorithms for each x-ray image. First one is based on Canny edge detection and second one on bothat filter. Canny edge detection is a specific edge detection algorithm and works well to detect contours of objects in our case markers. However, it can also detect any other objects in image, such as bones and -if present- even the catheter. Next, bothat filtering which is used our double check mechanism, is applied to the same images. Bothat filter performs a gray scale morphological operation,

which is essentially a closing operation (dilation followed by erosion) and a subsequent subtraction from the original image. Bothat filter is used to find intensity regions in an image. Assume that $\{p_{canny}\}$ are points found by canny edge detection and $\{p_{bothat}\}$ are points found by bothat filter. $\{p_{canny}\}$ were considered as center of a real marker, $\{p_{marker}\} \subset \{p_{canny}\}$, if there is a $\{p_{bothat}\}$ closely positioned to $\{p_{canny}\}$ less than a given threshold. False markers which are found by Canny edge detection were partially eliminated. Figure 2.2 shows markers detected by two method and initially identified false markers.

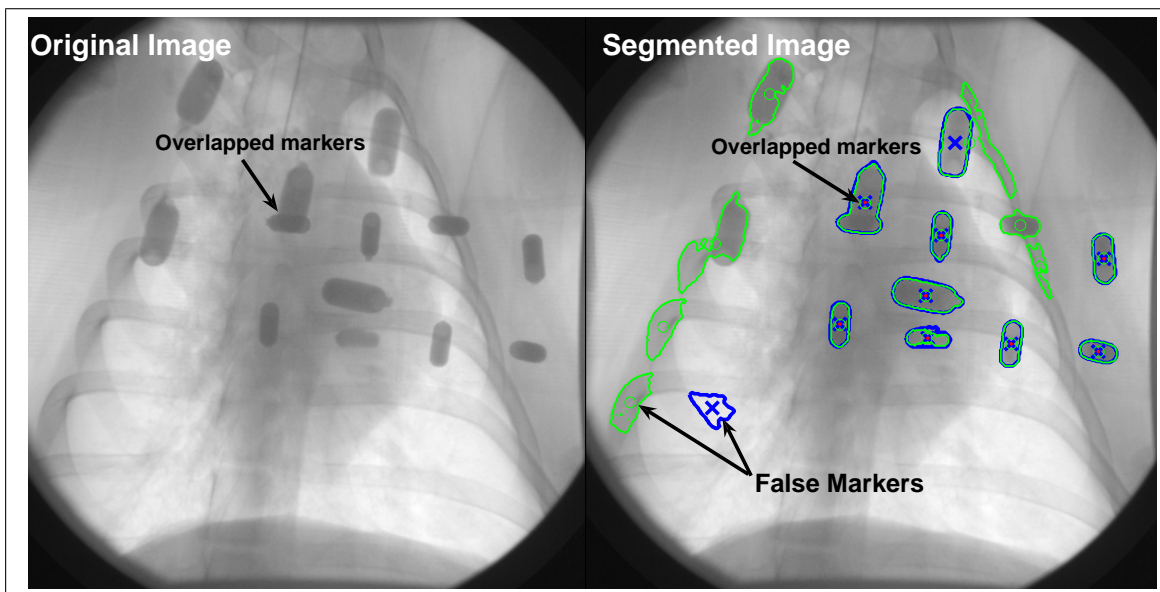


Figure 2.2 Distance between center of markers (X) detected by canny edge detection and center of markers (O) detected by bothat filter was determined. If centers are closer than a threshold then center of markers (X) detected by canny edge detection were assigned as a real marker(.)

Reconstruction of 3D position of markers in x-ray side requires finding correspondence between $\{p_{marker}\}$ markers in consecutive x-ray images. While determining marker center using canny edge detection, some properties, such as area and orientation of markers, were also measured and stored. These properties were utilized to find their correspondences among markers in the consecutive images. As it is mentioned above, C-arm rotates around the longitudinal axis, only primary angle is changed at each step. This implies that, for $\{p_{marker}\}_{i,n}$, i th marker in n th $\in \mathbb{N}$ x-ray image, its corresponding marker in $(n+1)$ th $\in \mathbb{N}$ x-ray image should be in a slightly shifted horizontal direction. Therefore, instead of comparing $\{p_{marker}\}_{i,n}$ with all $\{p_{marker}\}_{n+1}$,

properties of $\{p_{marker}\}_{i,n}$ were compared with properties of each $\{p_{marker}\}_{j,n+1}$ whose distance $d_{i,j}$, was smaller than a threshold value, R_{search} . R_{search} is defined experimentally and shown in Figure 2.3. Candidate markers within search area are shown in Figure 2.4. Comparison of markers was based on their area, orientation and vertical coordinate of markers in x-ray images and it is calculated by the following equation:

$$C_{i,j} = \frac{A_j}{A_i} * |O_j - O_i| * |y_j - y_i| \quad (2.1)$$

where i refers to marker in n th x-ray image and j refers to marker within R_{search} in $(n+1)$ th x-ray image and A is area of marker, O is orientation of marker, y is vertical coordinate of marker. High value of $C_{i,j}$ implies that these two markers corresponds to each other. This calculation was repeated for every marker in x-ray image $n \in \mathbb{N}$ and correspondence matrix, $CorrMat_n$, was built. Using $CorrMat$ for each frame, we reconstructed 3D location of marker in x-ray side.

2.2.2 MRI Side Fiducial Marker Detection

MRI was performed at Siemens Sonata 1.5T scanner. Position of markers in MRI side was determined by processing 3D T_1 - weighted gradient echo images. Detection of markers in 3D MR volume was performed in two steps. Since markers were attached to anterior and the posterior of the patient, 3D MR image is first divided into two parts. Maximum intensity projections (MIP) of each 3D MR volume and the initial division are shown in Figure 2.5. A marker detection algorithm was applied to each subvolume. First, a MIP trough coronal direction was obtained and segmentation was done by canny edge detection. Example of segmented markers is shown Figure 2.5. Centers of these segmented markers provides the 2D location of markers (x and y). Boundary of segmented marker was used to find coordinate in z direction. A line profile was then build from center of marker through the 3D volume. A masking operation is performed on that line to include the pixels within the boundary of given marker but exclude pixels outside. Through the z direction there were the most contagious bright pixel which were represent the given marker. Weighted location of pixels which were brighter than the gray threshold were used to find z coordinate of this marker. The

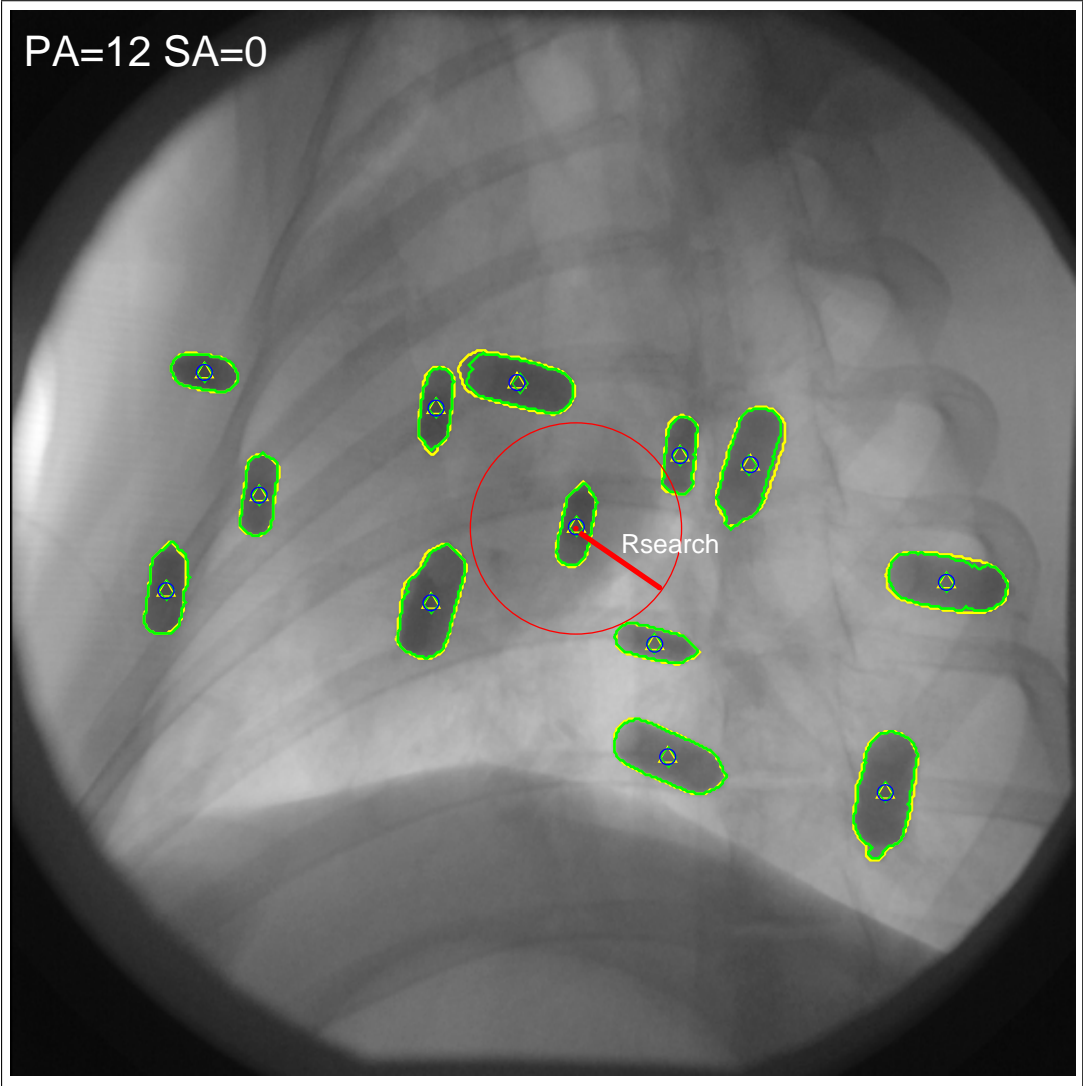


Figure 2.3 A search radius R_{search} is defined and a circle is constructed to find candidate markers in consecutive frame

following equation was applied

$$z = \frac{1}{N} \sum_{i=0}^N (\gamma_i * z_i) \tag{2.2}$$

where i refers to pixel index for the pixels with greater intensity then a threshold, γ is the intensity of that pixel. All three coordinates of a marker were found in MR image space, however they should be transferred to real space. This was achieved by multiplying each coordinates by its pixel spacing (z coordinate with slice thickness in z , we usually acquire isotropic in all axis) and applying a coordinate transformation.

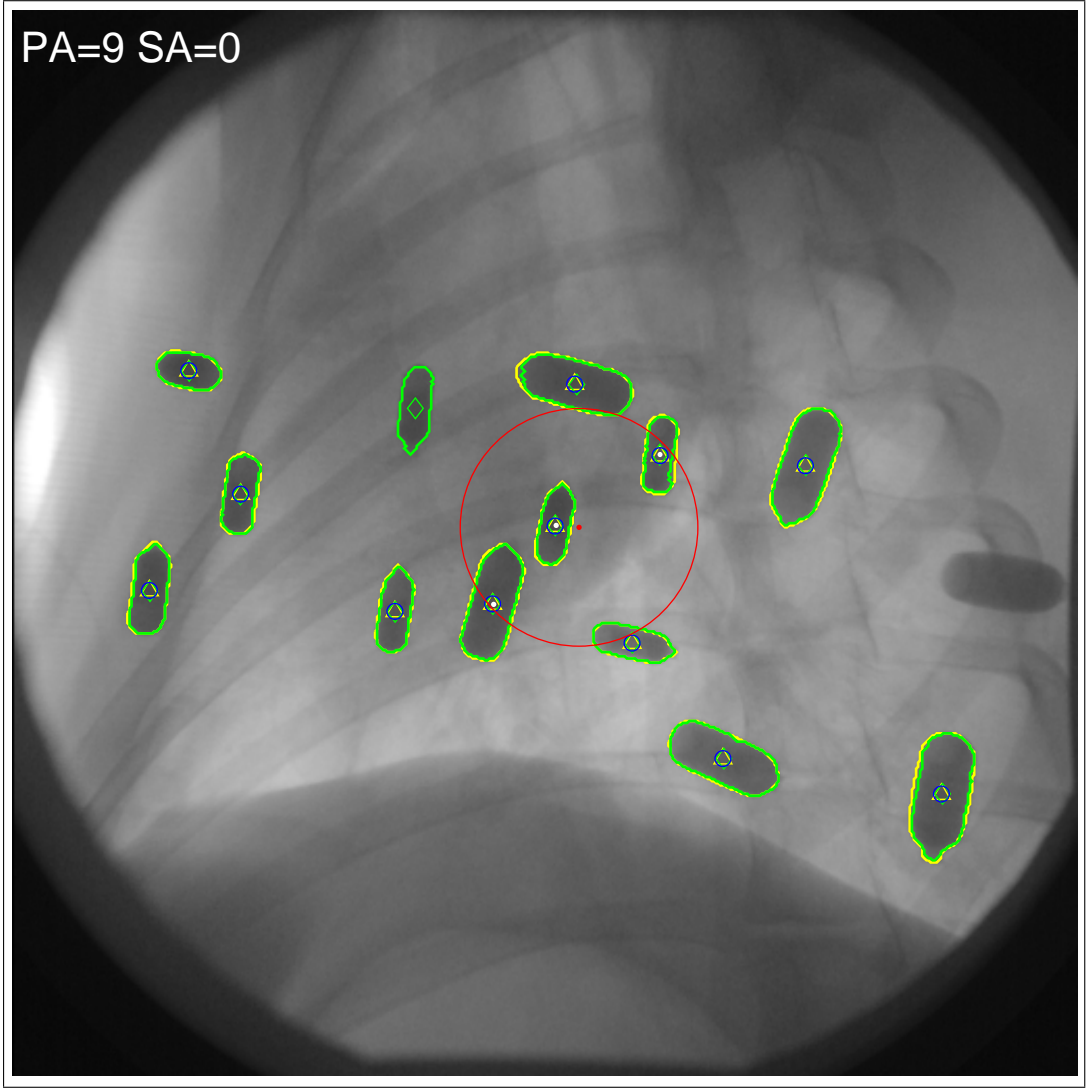


Figure 2.4 Markers with in the search circle are found and their properties are compared

Equation 2.3 was used to determine 3D location(x_{re}, y_{re}, z_{re}) of markers in MR space.

$$\begin{bmatrix} x_{re} \\ y_{re} \\ z_{re} \end{bmatrix} = \begin{bmatrix} x_{mr} \\ y_{mr} \\ z_{mr} \end{bmatrix} \begin{bmatrix} P_x \\ P_y \\ P_z \end{bmatrix} + \begin{bmatrix} T_x \\ T_y \\ T_z \end{bmatrix} \quad (2.3)$$

P_x, P_y, P_z are pixel spacings in directions x, y, z, respectively. T_x, T_y, T_z are parameters for translation from local 3D volume coordinate system space to MRI space in directions x, y, z, respectively.

The procedure was applied also for posterior part of 3D volume image and

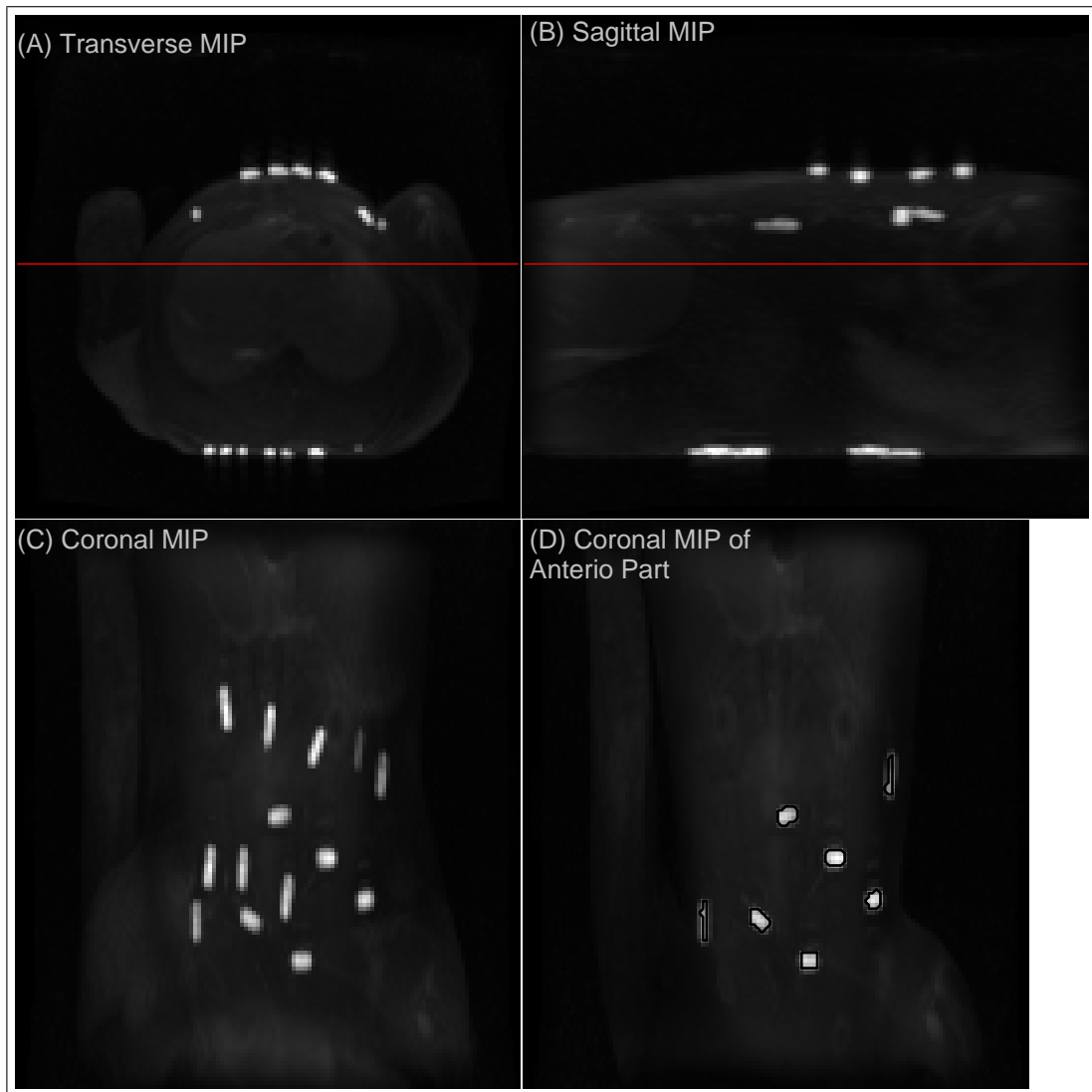


Figure 2.5 Maximum intensity projections of volumetric MR images on transverse (A), sagittal (B), coronal (C) direction and segmented markers (D)

markers at that part were detected. Combining these two marker set from anterior and posterior we obtain the whole set of 3D marker in MRI side.

2.2.3 Correspondence Between Two Point Sets

In previous two sections robust detection and 3D point reconstruction methods are described. In this section, we introduce a novel algorithm to find the correspondence between two point sets in 3D. We base our method on triangle similarity and cumulative confidence building to find best matching. Each 3 points in each set forms a different

triangle and all possible pairs of triangles are compared within the two groups (MR and XF). Two triangles are assumed to be similar if their sides are equal to each others. Let Δ_1 is triangle with sides (a_1, b_1, c_1) , it is similar Δ_2 to other triangle, Δ_2 , with sides (a_2, b_2, c_2) , there is this relationship between matching sides:

$$\frac{a_1}{a_2} = \frac{b_1}{b_2} = \frac{c_1}{c_2} = 1 \quad (2.4)$$

Then Δ_1 and Δ_2 are similar, we use the notation $\Delta_1 \sim \Delta_2$.

Since point sets found in previous chapters are not exactly at their true locations because of noise and two different imaging method, this similarity equation could be modified as follows:

$$S_{1,2} = |1 - \frac{a_1}{a_2}| + |1 - \frac{b_1}{b_2}| + |1 - \frac{c_1}{c_2}| \quad (2.5)$$

$S_{1,2}$ represent a similarity matrix of Δ_1 and Δ_2 . In ideal case $S_{1,2}$ is expected to equal zero.

Suppose we have two point sets with M and X number of points respectively with points $\{m_a, a = 1, 2, \dots, k\}$ and $\{x_i, i = 1, 2, \dots, l\}$. We form all possible triangles from these point sets and obtained triangle set P , where $\{p_b, b = 1, 2, \dots, m\}$ and R , where $\{r_j, j = 1, 2, \dots, n\}$. Number of triangles in P and R are the following:

$$m = \frac{k!}{(k-3)! * 3!} \quad (2.6)$$

$$n = \frac{l!}{(l-3)! * 3!} \quad (2.7)$$

Triangles in P were compared with triangles in R using the eq.2.5. If $S_{b,j}$ is smaller than the threshold, correspondence between triangles p_b and r_j is transferred to a big correspondence matrix $Corr$ with dimension $k \times l$. Comparison of two triangles based on 6 different orientations of them for a given pair and the minimum value with that specific orientation were considered best correspondence of two triangles. Orientation of triangles gives use the corner-to-corner matching which is actually point-

to-point or marker-to-marker match. If the minimum similarity is less than threshold, its cumulative match index is increased by one at the corresponding matrix locations after each similar triangle pair. The correspondence matrix *Corr* at the end shows "best confidence" correspondence between point sets *M* and *X*. The higher value in *Corr* indicates that that specific column and row are matching pairs. This information was used to complete the registration of x-ray and MRI side marker sets. Results of our segmentation approaches and matching algorithm will be explored in the next section.

2.3 Results

2.3.1 X-Ray Side Fiducial Marker Detection

X-Ray side automatic marker detection algorithm was tested in 10 animal experiments. Swines were used as subjects in all experiments and custom tight-fitting vest with embedded fiducial markers was employed to affix the fiducial markers on the swine body, as shown in Figure 2.1. The aim was to prevent any shift of the fiducial markers on loose skin. Previously markers are individually placed at predetermined locations with adhesive tapes. This was taking more time, and was more susceptible for unwanted marker motion. Beside the standard image acquisition for manual registration, a rotational acquisition was obtained for each subject to obtain 21 images from PA= -30° to PA= $+30^\circ$ with $\Delta\alpha=3^\circ$ angle increment. Automatic detection algorithm was applied to data sets and 3D position of markers were reconstructed. Number of markers seen in images, number of detected markers in x-ray side and computation times were recorded [Table 2.1]. In all 10 experiments 14-16 markers were visible and mean detection ratio with standard deviation for x-ray side markers was calculated as 95.1 ± 4.3 . Even all 21 x-ray images were used to detect the markers some of the markers were not detected but there were no false markers. The reason for undetected some obscure visible markers is some markers were not captured with sufficient images to reconstruct 3D point or correspondence between markers in consecutive frames was not established for these markers mainly because of too many overlapping cases. Verification of our results based on back projection of 3D reconstructed markers on each

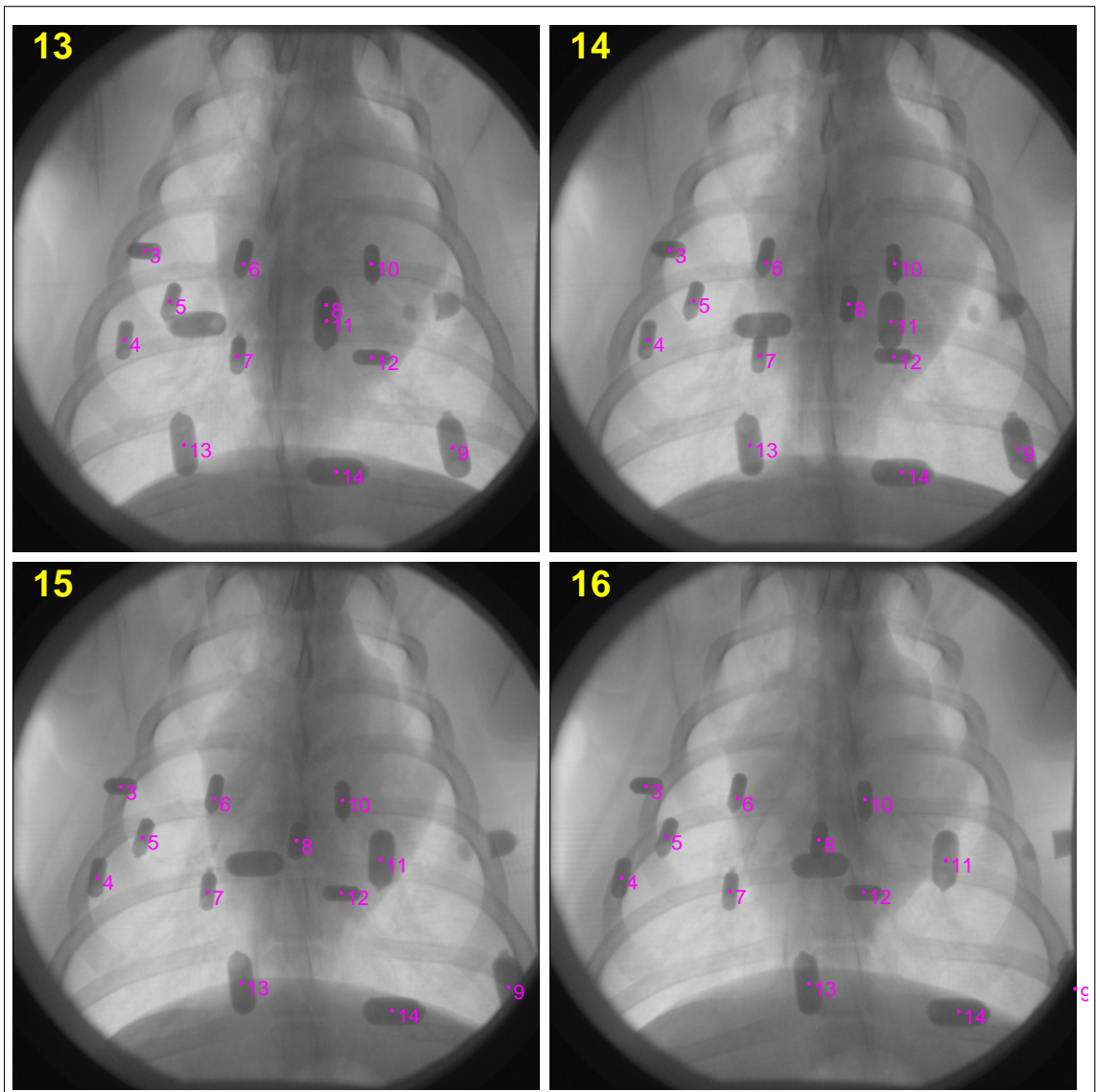


Figure 2.6 Detected and 3D reconstructed x-ray side fiducial markers are back projected to each frames to verify the results.

rotational frames, as seen in Figure 2.6.

As a small add-on experiment to our case 2, we used a half-rotational scan to test our algorithm, aiming to decrease radiation dose and detection time. Number of visible markers in this case was 14 and 3D reconstructed markers were 10. Detection ratio decreased to %71 from $PA=+15^\circ$ to $PA=-15^\circ$, image acquisition.

2.3.2 MRI Side Fiducial Marker Detection

Since required image set is the same with the manual one as it has been practiced in XFM, it does not require any additional image acquisitions for automatic detection routine. 3D gradient echo imaging was applied to subjects and 3D volumetric data was acquired. Automatic marker detection algorithm for MRI side was applied to 10 data sets. Number of detected MRI markers and elapsed times were recorded, as seen in Table 2.1. Except for the case 2, all markers were found for all cases. Detection ratio is $99.3 \pm 1.9\%$. 3D reconstructed markers are back projected on MIP images to visually check our results, as shown in Figure 2.7.

2.3.3 Correspondence Between Two Point Sets

We designed a general method to find the correspondence between two 3D point set. We applied our correspondence algorithm for 10 *in vivo* data after testing it in great detail in simulated data. *In vivo* results are shown in Table 2.1. Our method found correct correspondences in all experiments even if number of members for each set is not equal. There may be some points which does not have any correspondent in the other set, in these cases our method find correctly only all existent correspondences.

For simulation experiments, we created 3D point sets with arbitrary number of points and their coordinates randomly. We applied rotational and translational transformation to these point sets and also added some noise to simulate any possible noise coming from different image modalities. We run our algorithm using these two point sets. Simulated data results are shown in Table 2.2.

2.4 Discussion and Conclusions

X-ray fused with MRI (XFM) is a system which combines different characteristics of these image modalities, aiming to obtain excellent image guidance for minimally

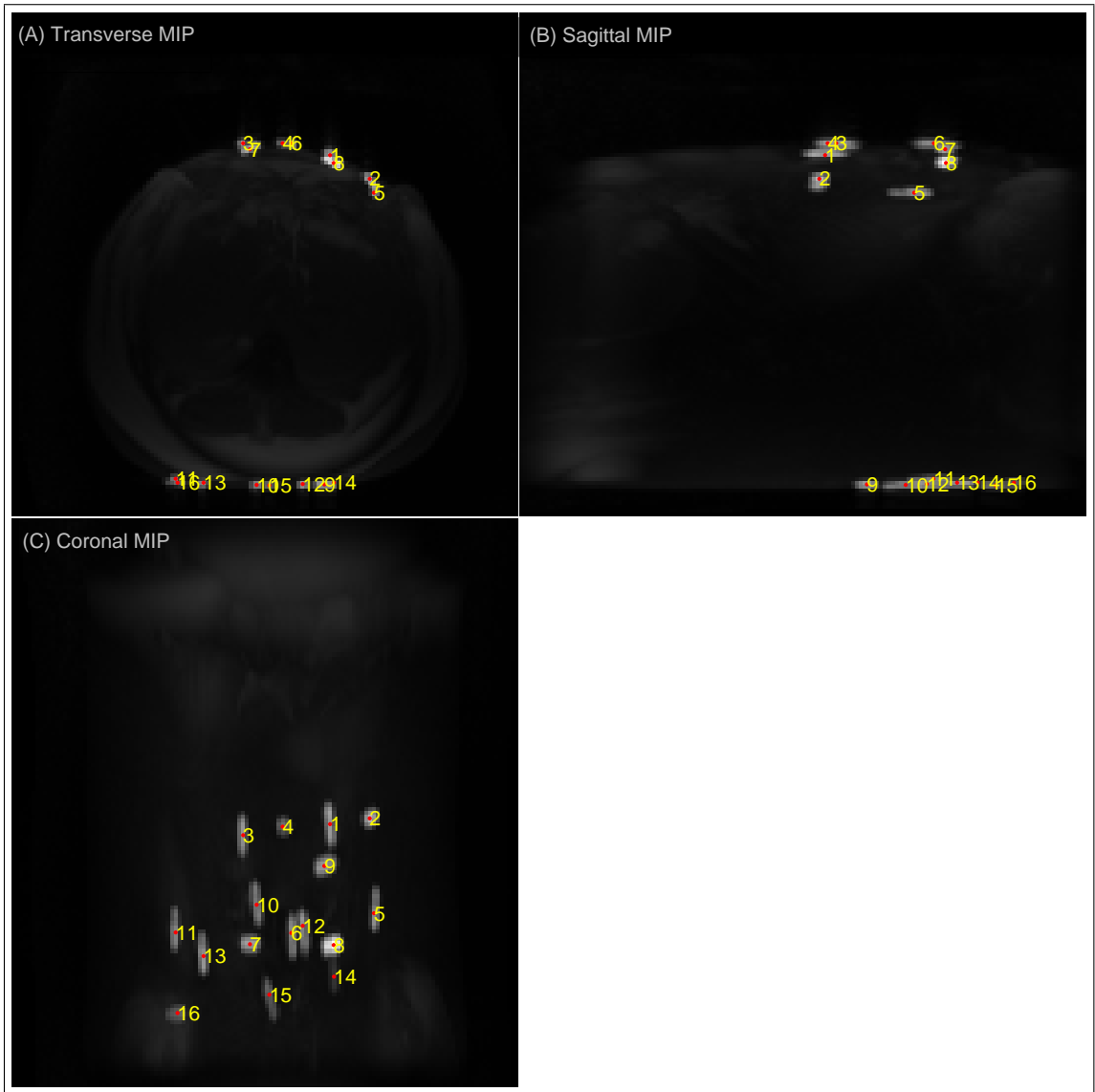


Figure 2.7 Automatically detected MRI side fiducial markers are back projected to MIP of 3D volume to verify the results.

Table 2.1

Automatic detection algorithm was tested, in vivo animal experiments. 16 ± 2 markers which are affixed to swine body by tight vest were employed in each experiments.

	# of marker	X-ray side markers		MRI side markers		Correspondence		Time
		detected	t (sec)	detected	t (sec)	# of corr.	t (sec)	t (sec)
Exp-1	14	14	64	14	31	14	7	102
Exp-2	14	10	32	14	22	10	2	56
Exp-3	16	15	64	15	23	14	7	94
Exp-4	16	15	64	16	23	15	7	94
Exp-5	14	13	64	14	24	12	5	94
Exp-6	16	14	64	14	25	12	6	95
Exp-7	16	15	64	16	24	14	8	98
Exp-8	16	16	64	16	24	16	9	97
Exp-9	16	15	64	16	24	15	7	95
Exp-10	15	15	64	15	24	15	7	95

invasive interventions. Fusion of these two images is achieved by registering x-ray and MRI images. External fiducial markers, which are attached to the both with tight-fitting vest, are used to complete registration process. These markers, which are visible in both images, were identified and reconstructed in 3D space for both x-ray and MRI. Identification algorithms were different for each images because of their image characteristic.

In x-ray images detection of markers were difficult because of frequent overlapping of markers. Therefore, multiple images were acquired from $PA=-30^\circ$ to $PA=+30^\circ$. Markers are detected and correspondences between them were found within different frames of the rotational x-ray image set. Using these correspondences markers were reconstructed in 3D [31]. Our method, detected almost all marker in 10 animal experiments. There were some markers which were not detected because of too many overlapping cases or insufficient frames to reconstruct these markers in 3D, but this did not stop our registration process.

Markers in MR images were located by detecting markers first in 2D after per-

Table 2.2

We created 3D point sets with arbitrary number of member and select some of them randomly. We applied rotational and translational transformation these selected points and also added some noise to simulate any possible noise coming from different image modalities

	# of points	# of selected points	Translation (x,y,z)	Rotation (x,y,z)	Noise (for each coordinates)	# of found corr.
Sim-1	10	5	(50, 50, 50)	($\pi/4$, $\pi/4$, $\pi/4$)	± 5 units	5
Sim-2	20	7	(50, 50, 50)	($\pi/4$, $\pi/4$, $\pi/4$)	± 5 units	7
Sim-3	20	13	(10, 20, 30)	($\pi/4$, $\pi/3$, $\pi/8$)	± 5 units	13
Sim-4	30	21	(30, 40, 20)	($\pi/5$, $\pi/6$, $\pi/7$)	± 5 units	21
Sim-5	40	32	(10, 20, 30)	($\pi/5$, $\pi/6$, $\pi/7$)	± 5 units	30

forming a MIP of 3D gradient echo image volume. Before that, 3D volume was first divided two parts as a anterior and posterior to simplify detection process. Segmentation algorithm was applied for these two coronal MIP images and 2 coordinates of marker were found. Third coordinate, in AP direction, was determined by weighted intensities of pixel within volume found by previous segmentation process. In some cases few visible markers were not detected because of noise in MR images.

Even if there were some undetected markers markers, our method for correspondence had excellent results that it found all possible correspondences in all experiments. Robustness of our matching algorithm comes from our innovative and simple solution for this problem. We used triangle similarity, which is simple and effective, to find correspondence between 3D point sets. Furthermore, a correspondence of two points from different sets were determined by not only one comparison but by many comparisons. This might be a time consuming approach for manual approach but perfect from a computer. If the number of points increase in both sets, this will cause an increased confidence in marker matching, because more triangle will be compared and contribute to correspondence matrix. *In vivo* experiments as shown in Table 2.1 displays that our approach performs well in our XFM system.

We also tested our matching algorithm with simulated data. We randomly generated 3D coordinates, set1, within (100,100,100) space. For second set, set2, we

chose some points randomly in arbitrary order. These points were translated and rotated many times with different parameters. Finally, noise was added to set2 to simulate a real XFM environment. Simulation results are shown in Table 2.2. In Sim-5, 2 correspondences were not found. The reason is that since set1 were generated randomly, these two points were so close to each other further noise was added on them which makes difficult to find correspondence between them. Since markers are uniformly placed around the body of patient to have minimum target registration error (TRE) [33], we do not have such problem.

We designed an elastic velcro tight-fitting vest to eliminate any shift of markers due to loose skin. Elastic fabric provides tight placement of markers around the body, further it allows us to use vest with different sized patient. In addition, placement of markers is fast and standardized with this tight-fitting vest.

3. Clinical Applications

Our developed automatic registration system was also tested in various clinical studies. The clinical protocol (NCT00064896) was approved by the NHLBI Institutional Review Board. Consecutive patients undergoing invasive procedures were invited to participate. All subjects consented to participate in writing and were investigated and treated at the NIH Clinical Center in Bethesda, MD, US.

3.1 Baseline MRI

MRI was performed at 1.5 T (Sonata, Siemens) using an eight channel phased array surface coil (Nova Medical). Gadopentate dimeglumine (Magnevist, Berlex) 0.2 mmol/kg was administered for contrast enhanced examinations. Cardiac regions of interest were contoured from multiple, breath-held, electrocardiogram (ECG)-gated cine steady-state free precession (SSFP) MRI using the following typical parameters: TR/TE (time to echo), 3.6/1.8 ms; flip angle, 65°; FOV, 300 mm × 244 mm; matrix, 256 × 127 pixels; slice thickness, 8 mm; bandwidth, 1085 Hz/pixel. Arterial adventitial and luminal contours were derived from 3D contrast-enhanced MRA (typical parameters: TR/TE, 2.3/0.9 ms; flip angle, 25°; FOV, 512 × 314 × 122 mm matrix, 256 × 156 × 54; bandwidth 815 Hz/pixel), from 3D breath-held T1- weighted MRI (typical parameters: TR/TE, 6.2/2.3; flip angle, 12°; FOV 400 × 325 × 220 mm matrix 256 × 156 × 64; bandwidth, 200 Hz/pixel), and/or a high resolution reduced field of view (FOV) technique [34]. External fiducial markers were located using 3D T1- weighted gradient echo (T1W-GRE) using the following typical parameters: TR/TE, 2.37/1.18 ms; flip angle, 17°; FOV, 400 × 300 × 230 mm; matrix, 256 × 192 × 61 voxels; bandwidth, 1300 Hz/pixel. MRI gradient warping distortion was corrected at the scanner console [35]. Images were transferred to a commercial workstation for manual segmentation of regions of interest then transferred to the XFM workstation within 15 min.

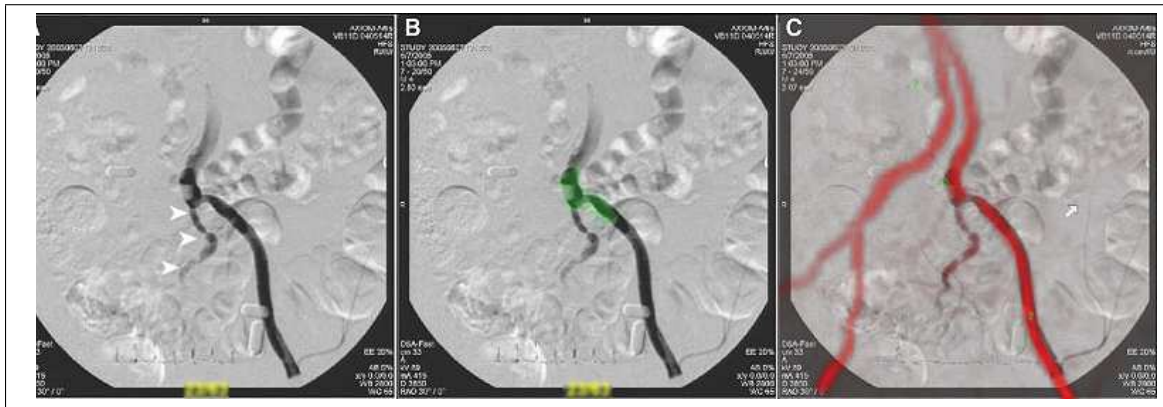


Figure 3.1 XFM using a 3D contrast-enhanced MR angiogram. (A) shows a retrograde L iliac radiocontrast angiogram in a contralateral oblique projection. (B) shows the regions of interest (adventitial borders, green) derived from a T1-weighted noncontrast MRI. (C) shows the XFM of both x-ray and MR angiograms. The correspondence is high.

3.2 Results

Twenty procedures were conducted in 19 subjects having a median age of 66 (range 23-82). Eight were femoropopliteal revascularization procedures (six recanalization for occlusion), six were iliac procedures (three recanalization for occlusion), and six were diagnostic cardiac procedures (two including coronary grafts, one for native coronary arteries only, one pericardiocentesis, and two myocardial mass).

3.2.1 Case Example: Roadmaps From Contrast-Enhanced MR Angiograms

XFM using roadmaps from MR angiography provides a simple test of correspondence. Clinically, this can reduce exposure to iodinated radiocontrast and possibly ionizing radiation. Figure 3.1 demonstrates a roadmap derived from 3D contrast-enhanced magnetic resonance angiography under XFM during conventional iliac angiography. Unlike conventional radiocontrast roadmapping, these roadmaps remain valid even as x-ray angulation was altered and even after table panning. In this case, the registration error was 1.6 mm RMS.

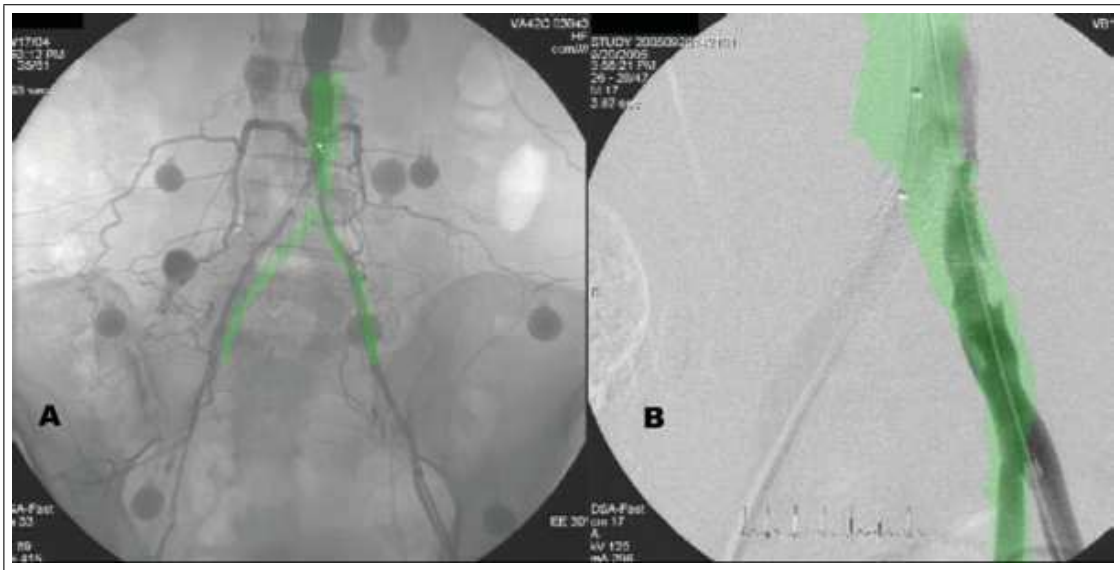


Figure 3.2 Unsatisfactory registration during an iliac artery revascularization procedure. Panel A shows the misregistration of a contrast-enhanced MR angiogram with x-ray during XFM. Multiple fiducial markers are positioned on the abdominal skin. Panel B shows another patient with MR-derived arterial adventitial contours overlaid during recanalization of occlusive iliac in-stent restenosis. Both presumably reflect error introduced by nonrigid deformation and respiratory motion of the fiducial markers.

3.2.2 Case Examples: Iliac Artery Revascularization and Registration Error

However, XFM did not provide consistently satisfactory roadmaps during iliac artery recanalization and angioplasty procedures. Figure 3.2 demonstrates two procedures during which registration was inadequate to guide catheter-based treatment. Figure 3.2A shows misregistered lumen contours from MR angiography. Figure 3.2B shows misregistered adventitial contours from breath-held MRI in another patient. The overall mean registration error was 3.5 ± 1.9 mm RMS and probably was exacerbated by the displacement of animal between two image scan. Registration error did not correlate with body mass index ($r^2 = 0.11$). Registration was similarly unsatisfactory (noncorrespondence of the parietal pericardial contour) during pericardiocentesis, in which MRI was performed in a supine position but the invasive procedure was performed with the torso elevated by 35° .

3.2.3 Case Example: Coronary Arteriography, Ventriculography, and ECG-Gated XFM

XFM coregistration of MRI and x-ray fluoroscopy was tested in this patient undergoing transfemoral left ventriculography and selective injections of coronary artery bypass grafts. Endocardial and epicardial contours of the left ventricle were obtained at multiple phases of the cardiac cycle. These contours were synchronized with the real-time ECG during radiocontrast angiography as shown in Figure 3.3. The MRI-derived endocardial border corresponded qualitatively with the radiocontrast ventriculogram, although the registration error was 5.2 mm RMS. During selective arteriography, for example of a right internal mammary to left anterior descending coronary artery bypass graft, MRI-derived regions of interest were appropriately represented dynamically during extensive table panning across multiple fields of view. In another representative patient, regions of interest such as myocardial infarction are displayed in context with the radiocontrast coronary arteriograms. The superposition of MRI regions of interest during table panning, even when x-ray fluoroscopy was not in use, enabled radiation-free positioning of the patient and x-ray gantry for subsequent acquisitions.

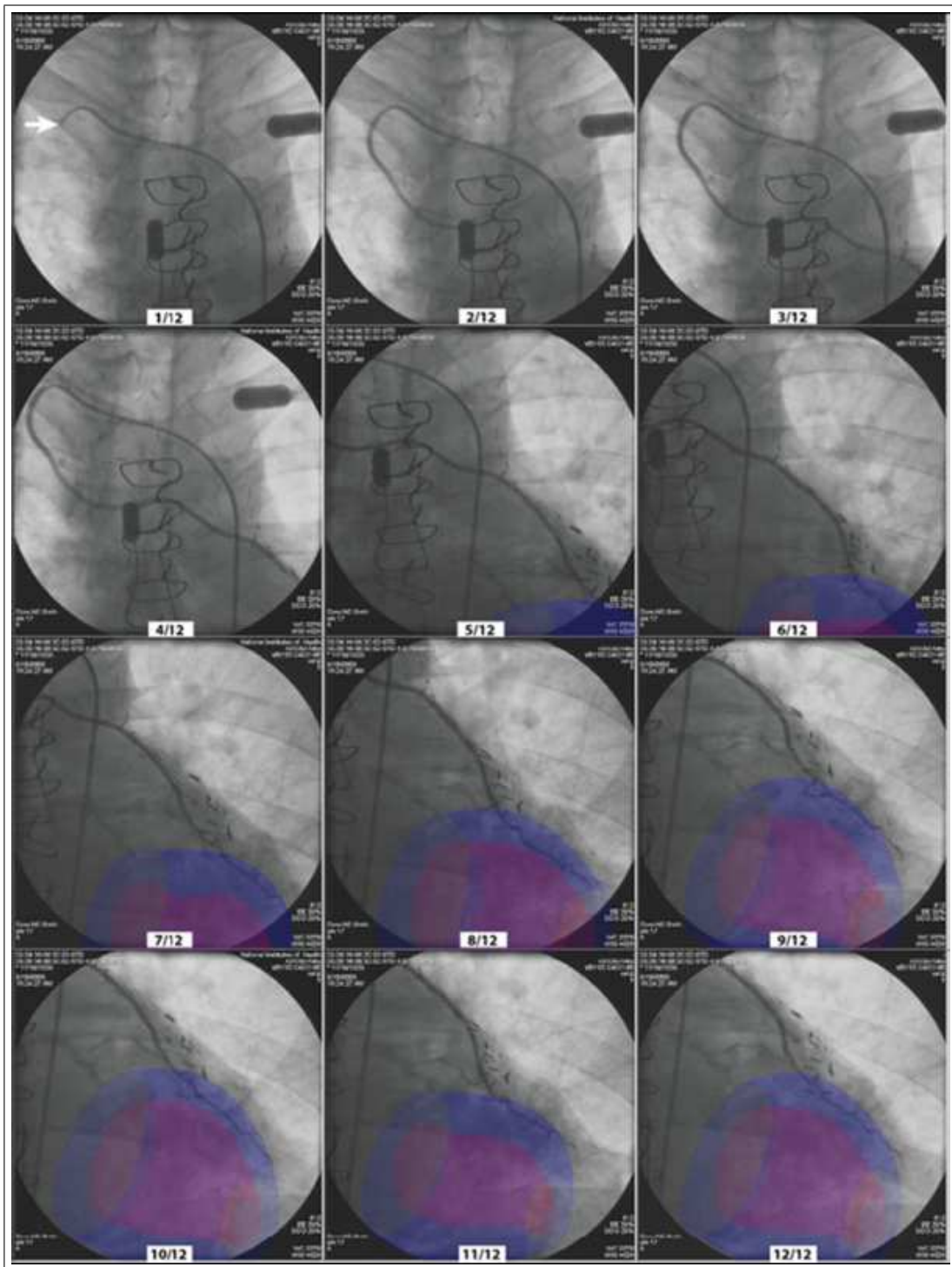


Figure 3.3 XFM during graft coronary arteriography. An injection sequence of a right internal mammary artery during ECG-gated XFM with continuous table panning. The corresponding numbered phase of the cardiac cycle is correctly represented by the MRI-derived regions of interest, irrespective of table position, throughout the injection.

4. Conclusion

Image fusion techniques have been developing to achieve better outcome of various minimal invasive procedures , to increase quality of diagnosis and to decrease hospitalization. X-ray fused with MRI is an innovative solution for catheter-based interventions. Drawbacks of each x-ray and MR imaging modalities are eliminated by combining these two complementary images. X-ray has high temporal and spatial resolution, on the other hand, MRI offers soft tissue contrast and 3D anatomic images.

Fusion of x-ray and MR images is achieved by registering two image sets. In general, there are different registration techniques for image fusion depending on the application. Intensity-based registration relies on same image contrast mechanism (like x-ray and CT) and algorithm works to find best similarity between two images by comparing intensities of images while seeking best rigid body transformation between them. Since x-ray and MR images have completely different image characteristic we can not apply this method for registration of x-ray and MR images. Feature-based registration uses extracted features from images and finds correspondence between these features to complete registration. However, feature detection and extraction requires reliable processes to find exact features which exist in both image sets. This is usually done manually or with supervision and is time consuming. On the other hand, point-based registration is the most accurate, fast and robust technique which is used as gold standard to evaluate other registration techniques. External fiducial markers or internal landmarks could be used to perform registration. For most of the applications, there are not adequate internal fiducial point markers that can be seen in both modalities for a successful registration. The major disadvantage of point-based registration is that it is vulnerable to movement of marker in loose skin when they are attached to the external surface of the body as it is the case in this thesis work.

In our study we used external fiducial markers which are attached to body with tight-fitting vest to minimize any shift in marker positions. For a successful regis-

tration, markers should be identified in both image sets and correct correspondence must be established. We implemented segmentation methods which identify markers in both x-ray and MR image sets and a novel matching algorithm to find correspondence between two point sets. Marker in x-ray images are detected and identified using multiple images. Multiple images are acquired with a single rotational scan to overcome overlapping of markers. In MRI side, markers are detected and identified using maximum intensity projections of a 3D T_1 - weighted echo gradient image set. Our proposed algorithm to find correspondence of marker sets from x-ray and MRI is actually a general solution to find correspondence between 3D point sets. Correspondence can be found even there are missing or false candidate points in point sets. Experimental and simulation results validate that our marker matching method works effectively.

In clinical studies we also have satisfactory results. We applied our methods in 19 different clinical cases. In first case, MR angiograms were projected on x-ray images and guided the catheter in revascularization procedures. Registration error was 1.6 mm RMS which is tolerable error for this procedure. In second case, we did not have satisfactory results because of movement of patient. Procedure was iliac artery recanalization and angioplasty procedure. The overall registration error was 3.5 ± 1.9 mm RMS. Coronary arteriography and ventriculography were the third clinical case and error was 5.2 mm RMS which is tolerable.

As a summary, as part of this thesis work, we developed automatic marker detection algorithms for both x-ray and MR images, find a general solution for correspondence between 3D point sets, design a marker placement system to improve the quality of registration and developed user interface for the clinical end-users. Our methods were tested extensively on animal experiments and used in several clinical studies. The overall performance of our additions and XFM in general seems satisfactory for many clinical studies.

4.1 Future Works

As described in Section 1.2, many medical image registration methods exist, and each has strength and weakness. A better method would be combining more than two modalities. A rough registration may be performed with point-based registration first and fine-tuned later using feature-based and intensity based methods as scenes change due to catheter manipulations and MR roadmap is simply old.

Another tool is currently needed to use prior acquired 3D images without markers to use with XFM. CT and MR images are usually acquired for diagnoses purposes and previously acquired image sets without markers may be used in XFM by registering them first with a standard MRI marker localization image acquired just before the intervention. Prior images (without markers) are registered with MR images (with markers) by using intensity or feature based registration method and x-ray image are overlaid with projection of reconstructed structures from prior CT or MR images. With this approach long scans, unnecessary repeats of imaging at the intervention day is avoided.

APPENDIX A. Algorithm of Finding Correspondence Between 3D Point Sets

The following algorithm is applied to two 3D point set:

```

for b=1:m
  if b=(equilateral triangle) || b=(isosceles triangle)
    break; %skip this triangle
  else
    for j=1:n
      if j=(equilateral triangle) || j=(isosceles triangle)
        break; %skip this triangle
      else
        S(1)=|1-(a1/a2)|+|1-(b1/b2)|+|1-(c1/c2)|
        S(2)=|1-(a1/a2)|+|1-(b1/c2)|+|1-(c1/b2)|
        S(3)=|1-(a1/b2)|+|1-(b1/a2)|+|1-(c1/c2)|
        S(4)=|1-(a1/b2)|+|1-(b1/c2)|+|1-(c1/a2)|
        S(5)=|1-(a1/c2)|+|1-(b1/b2)|+|1-(c1/a2)|
        S(6)=|1-(a1/c2)|+|1-(b1/a2)|+|1-(c1/b2)|
        [Smin,ind]=min(S)
        if Smin<threshold
          %find which sides constructed these triangles
          %let say 'a' in one set and 'i' in other set
          Corr(a,i)=Corr(a,i)+(threshold-Smin)
        end
      end
    end
  end
end
end

```

m is the number of triangle in one set and n is the number of triangle in other set. We did not compare equilateral triangle and isosceles triangle because they may contribute

false correspondences. Two triangles are compared with all possible orientations, which is 6. If minimum value, S_{min} , is smaller than the threshold, this value is added to correspondence of points 'a' and 'i' assuming that these points participate in construction of triangles. Since there are 3 points in one triangle S_{min} contributes 3 two points correspondence.

APPENDIX B. Auto-Registration User Interface

We developed a user interface for end-user to perform automatic registration and also to verify the position of markers by back projection 3D markers on x-ray or MR images. User interface is as shown in Figure B.1. User is needed to enter the locations of x-ray data and MRI data to perform registration. Function of each button is as follows:

- **Browser** : defines location of saved x-ray or MR data
- **Get Listener Param** : gets table position
- **Find Xray Marker** : runs the x-ray side marker detection algorithm
- **Show Xray Images** : displays x-ray image
- **Load Calibration** : gets the calibration parameters
- **Show Markers** : projects 3D x-ray side markers on x-ray images
- **Multi Images** : shows 4 x-ray images at the same time
- **Find Mri Marker** : runs the MRI side marker detection algorithm
- **Show MRI Marker** : displays 3D projection of MRI side markers on MIP
- **Save MRI Points** : saves 3D location of marker on hard disk
- **REGISTRATION** : runs the correspondence algorithm and registration algorithm



Figure B.1 Figure shows user interface for end-user to perform automatic registration process.

REFERENCES

1. Gianfelice, D., L. Lepanto, P. Perreault, C. Chartrand-Lefebvre, and P. Milette, "Value of ct fluoroscopy for percutaneous biopsy procedures," *J Vasc Interv Radiol*, Vol. 11, pp. 879–884, Jul 2000.
2. White, C. S., C. A. Meyer, and P. A. Templeton, "Ct fluoroscopy for thoracic interventional procedures," *Radiol Clin North Am.*, Vol. 38, pp. 303–322, Mar 2000.
3. Silverman, S. G., K. Tuncali, D. F. Adams, R. D. Nawfel, K. H. Zou, and P. F. Judy, "Ct fluoroscopy-guided abdominal interventions: techniques, results, and radiation exposure," *Radiology*, Vol. 212, pp. 673–681, Sep 1999.
4. Law, E. M., A. F. Little, and J. C. Salanitri, "Non-vascular intervention with real-time ct fluoroscopy," *Australas Radiol.*, Vol. 45, pp. 109–112, May 2001.
5. Paulson, E. K., D. H. Sheafor, D. S. Enterline, H. P. McAdams, and T. T. Yoshizumi, "Ct fluoroscopy-guided interventional procedures: techniques and radiation dose to radiologists," *Radiology*, Vol. 220, pp. 161–167, Jul 2001.
6. Stoeckelhuber, B. M., E. Schulz, U. H. Melchert, J. Blobel, J. Gellissen, H. Gehl, H. D. Weiss, and T. Leibecke, "Procedures, spectrum and radiation exposure in ct-fluoroscopy," *Rontgenpraxis*, Vol. 55, no. 2, pp. 51–57, 2003.
7. Fritz, J., and P. L. Pereira, "Mr-guided pain therapy: principles and clinical applications," *Rofo*, Vol. 179, pp. 914–924, Sep 2007.
8. Schulz, T., R. B. Tröbs, J. P. Schneider, W. Hirsch, S. Puccini, F. Schmidt, and T. Kahn, "Pediatric mr-guided interventions," *Eur J Radiol.*, Vol. 53, pp. 57–66, Jan 2005.
9. Graham, J. J., R. J. Lederman, and A. J. Dick, "Magnetic resonance imaging and its role in myocardial regenerative therapy," *Regen Med.*, Vol. 1, pp. 347–355, May 2006.
10. Spuentrup, E., A. Ruebben, T. Schaeffter, W. J. Manning, R. W. Günther, and A. Buecker, "Magnetic resonance-guided coronary artery stent placement in a swine model," *Circulation*, Vol. 105, pp. 874–879, Feb 2002.
11. Godart, F., J. P. Beregi, and L. Nicol, "Mr-guided balloon angioplasty of stenosed aorta: in vivo evaluation using near-standard instruments and a passive tracking technique," *J Magn Reson Imaging*, Vol. 12, pp. 693–644, 2000.
12. Omary, R. A., R. Frayne, and O. Unal, "Mr-guided angioplasty of renal artery stenosis in a pig model: a feasibility study," *Vasc Interv Radiol*, Vol. 11, pp. 373–381, 2000.
13. Buecker, A., J. M. Neuerburg, and G. B. Adam, "Real-time mr fluoroscopy for mr-guided iliac artery stent placement," *J Magn Reson Imaging*, Vol. 12, no. 616–622, 2000.
14. Kuehne, T., M. Saeed, and C. B. H. CB, "Endovascular stents in pulmonary valve and artery in swine: feasibility study of mr imaging-guided deployment and postinterventional assessment," *Radiology*, Vol. 226, pp. 475–481, 2003.
15. Jones, D., D. A. Christopherson, J. T. Washington, M. D. Hafermann, J. W. Rieke, J. J. Travaglini, and S. S. Vermeulen, "A frameless method for stereotaxic radiotherapy," *Br. J. Radiol.*, Vol. 66, pp. 1142–1150, 1993.

16. Maurer, C. R., J. M. Fitzpatrick, M. Y. Wang, R. L. Galloway, R. J. Maciunas, and G. S. Allen, "Registration of head volume images using implantable fiducial markers," *IEEE Trans. Med. Imag.*, Vol. 16, pp. 447–462, Aug 1997.
17. Taylor, R. H., B. D. Mittelstadt, H. A. Paul, W. Hanson, P. Kazanzides, J. F. Zuhars, B. Williamson, B. L. Musits, E. Glassman, and W. L. Bargar, "An image-directed robotic system for precise orthopaedic surgery," *IEEE Trans. Robot. Automat.*, Vol. 10, pp. 261–275, June 1994.
18. Weese, J., G. P. Penny, P. Desmedt, T. M. Buzug, D. L. G. Hill, and D. J. Hawkes, "Voxel-based 2-d/3-d registration of fluoroscopy images and ct scans for image-guided surgery," *IEEE Trans. Inform. Technol. Biomed.*, Vol. 1, pp. 284–293, Dec 1997.
19. Lemieux, L., R. Jagoe, D. R. Fish, N. D. Kitchen, and D. G. T. Thomas, "A patient-to-computed-tomography image registration method based on digitally reconstructed radiographs," *Med. Phys.*, Vol. 21, pp. 1749–1760, 1994.
20. Wein, W., *Intensity Based 2D-3D registration Algorithms for Radiation Therapy*. PhD thesis, Munich University, Munich, 2003.
21. LaRose, D., J. Bayouth, and T. Kanade, "Transgraph: Interactive intensity-based 2d/3d registration of x-ray and ct data," *Proc. SPIE*, Vol. 3979, pp. 385–396, 2000.
22. Weese, J., R. Göcke, G. P. Penny, P. Desmedt, T. M. Buzug, and H. Schumann, "Fast voxel-based 2d/3d registration algorithm using a volume rendering method based on the shear-warp factorization," *Proc. SPIE*, Vol. 3661, pp. 802–810, 1999. Medical Imaging 1999.
23. Kita, Y., D. L. Wilson, and J. A. Noble, "Real-time registration of 3d cerebral vessels to x-ray angiograms," *In MICCAI*, pp. 1125–1133, 1998.
24. McLaughlin, R. A., J. Hipwell, G. P. Penney, K. Rhode, and A. Chung, "Intensity-based registration versus feature-based registration for neurointerventions," *Proc. Medical Image Understanding and Analysis*, 2001.
25. Kapoor, V., B. M. McCook, and F. S. Torok, "An introduction to pet-ct imaging," *RadioGraphics*, Vol. 24, no. 2, pp. 523–543, 2004.
26. Fahrig, R., K. Butts, J. A. Rowlands, R. Saunders, J. Stanton, G. M. Stevens, B. L. Daniel, Z. Wen, D. L. Ergun, and N. J. Pelc., "A truly hybrid interventional mr-xray system: feasibility demonstration.," *J Magn Reson Imaging*, Vol. 13, pp. 294–300, Feb 2001.
27. Fahrig, R., G. Heit, Z. Wen, B. L. Daniel, K. Butts, and N. J. Pelc., "First use of a truly-hybrid x-ray mr imaging system for guidance of brain biopsy," *Acta Neurochir*, Vol. 145, no. 11, pp. 995–997, 2003. Case Reports.
28. Yu, H., R. Fahrig, and N. J. Pelc., "Co-registration of x-ray and mr fields of view in a hybrid xmr system," *J Magn Reson Imaging*, Vol. 22, pp. 291–301, Aug 2005.
29. Rhode, K. S., D. L. G. Hill, P. J. Edwards, J. Hipwell, D. Rueckert, G. Sanchez-Ortiz, S. Hegde, V. Rahunathan, and R. Razavi, "Registration and tracking to integrate x-ray and mr images in an xmr facility," *IEEE Trans. Med. Imaging*, Vol. 22, pp. 1369–1378, Nov 2003.

30. K.S. Rhode, M. Sermesant, S. H. G. S.-O. D. R. R. R., and D. Hill., “and d.l.g. hill. xmr guided cardiac electrophysiology study and radio frequency ablation,” *In Proc. SPIE Med. Imaging*, Vol. 5369, pp. 10–21, 2004.
31. Gutierrez, L. F., *X-ray Fused with MRI (XFM) for Guidance of Catheter-Based Interventions*. PhD thesis, Johns Hopkins University, Baltimore, 2005.
32. Gutierrez, L. F., R. J. Lederman, E. R. McVeigh, and C. Ozturk, “Sparsely sampled distortion correction for a c-arm mounted x-ray image intensifier,” *Medical Physics*, 2007.
33. Fitzpatrick, J. M., J. B. West, and C. R. J. Maurer, “Predicting error in rigid-body point-based registration,” Vol. 17, pp. 694–702, Oct 1998.
34. Sampath, S., A. N. Raval, R. J. Lederman, and E. R. McVeigh, “High-resolution 3d arteriography of chronic total peripheral occlusions using a t1-w turbo spin-echo sequence with inner-volume imaging,” *Magn Reson Med*, Vol. 57, pp. 40–49, 2007.
35. Jovicich, J., S. Czanner, D. Greve, E. Haley, and A. vanderKouwe, “Reliability in multi-site structural mri studies: Effects of gradient non-linearity correction on phantom and human data.,” *Neuroimage*, Vol. 30, pp. 436–443, 2006.